PLASMONIC BAND GAP CAVITIES

A DISSERTATION SUBMITTED TO

THE DEPARTMENT OF PHYSICS

AND THE INSTITUTE OF ENGINEERING AND SCIENCE

OF BILKENT UNIVERSITY

IN PARTIAL FULFILLMENT OF THE REQUIREMENTS

FOR THE DEGREE OF

DOCTOR OF PHILOSOPHY

By

Aşkın Kocabaş

July, 2008

I certify that I have read this thesis and that in my opinion it is fully adequate, in scope and in quality, as a dissertation for the degree of doctor of philosophy.

Prof. Dr. Atilla Aydınlı

I certify that I have read this thesis and that in my opinion it is fully adequate, in scope and in quality, as a dissertation for the degree of doctor of philosophy.

Prof. Dr. Abdullah Atalar

I certify that I have read this thesis and that in my opinion it is fully adequate, in scope and in quality, as a dissertation for the degree of doctor of philosophy.

Prof. Dr. Raşit Turan

I certify that I have read this thesis and that in my opinion it is fully adequate, in scope and in quality, as a dissertation for the degree of doctor of philosophy.

Assoc. Prof. Dr. Oğuz Gülseren

I certify that I have read this thesis and that in my opinion it is fully adequate, in scope and in quality, as a dissertation for the degree of doctor of philosophy.

Asst. Prof. Dr. Ömer İlday

Approved for the Institute of Engineering and Science:

Prof. Dr. Mehmet B. Baray
Director of the Institute

ABSTRACT

PLASMONIC BAND GAP CAVITIES

Aşkın Kocabaş

PhD in Physics

Supervisor: Prof. Dr. Atilla Aydınlı

July, 2008

Surface plasmon polaritons (SPP's) are trapped electromagnetic waves coupled to free electrons in metals that propagate at the metal-dielectric interfaces. Due to their surface confinement and potential in sub-wavelength optics, SPP's have been extensively studied for sensing and nanophotonic applications. Dielectric structures and metallic surfaces, both periodically modulated, can form photonic band gaps. Creating a defect cavity region in the periodicity of dielectrics allows specific optical modes to localize inside a cavity region. However, despite the demonstration of numerous plasmonic surfaces and unlike its dielectric counterparts, low index modulation in metallic surfaces limits the formation of plasmonic defect cavity structures. This thesis describes new approaches for plasmonic confinement in a cavity through the use of selective loading of grating structures as well as through the use of Moiré surfaces. In our first approach, we demonstrate that a high dielectric superstructure can perturb the optical properties of propagating SPPs dramatically and enable the formation of a plasmonic band gap cavity. Formation of the cavity is confirmed by the observation of a cavity mode in the band gap both in the infrared and the visible wavelengths. In addition to the confinement of SPP's in the vertical direction, such a cavity localizes the SPP's in their propagation direction. Additionally, we have demonstrated that such biharmonic grating structures can be used to enhance Raman scattering and photoluminescence (PL). Using biharmonic grating structure 10^5 times

enhancement in Raman signal and 30 times enhancement in PL were measured. Furthermore, we show that metallic Moiré surfaces can also serve as a basis for plasmonic cavities with relatively high quality factors. We have demonstrated localization and slow propagation of surface plasmons on metallic Moiré surfaces. Phase shift at the node of the Moiré surface localizes the propagating surface plasmons in a cavity and adjacent nodes form weakly coupled plasmonic cavities. We demonstrate group velocities around $v = 0.44c$ at the center of the coupled cavity band and almost zero group velocity at the band edges can be achieved. Furthermore, sinusoidally modified amplitude about the node suppresses the radiation losses and reveals a relatively high quality factor for plasmonic cavities.

ÖZET

Aşkın Kocabaş

PLAZMON BANT ARALIĞI KOVUKLARI

Fizik Doktora

Tez Yöneticisi: Prof. Dr. Atilla Aydınlı

Temmuz, 2008

Yüzey plazmonları, metal ve dielektrik ortamlarının arayüzlerinde hareket eden, metallerde ki serbest elektronlara çiftlenmiş elektromanyetik bir dalgadır. Yüzeyde yerelleşmiş olmalarından ve dalga boyundan daha küçük ölçekte uygulanabilir olmasından dolayı, yüzey plazmonları çeşitli algılayıcı ve nano boyutlu optik uygulamalarda geniş bir şekilde kullanılmaya başlanmıştır. Periyodik şekilde biçimlendirilmis dielektrik ve metal yüzeyler ışığın yayılamayacağı yasaklı bant aralıkları oluşturabilirler. Bu periyodik yapılarda periyodun bozulduğu kusurlu alanlar oluşturularak belirli dalga boylarındaki ışığın bu bölgelerde hapsedilmesi sağlanabilir. Dielektrik tabanlı bu tür yapıların bugüne kadar gösterilmiş olmasına rağmen benzer biçimdeki metal yüzeylerin kırılma sabitinin çok az değişim gostermesi, metal yüzeylerde plazmonlar için kusurlu kovuk elde edilmesini engeller. Bu tez, yüzey plazmonlarını hapsetmek için, çift periyodik yüzeylerin belirli bölgelerinin yüksek dielektrik malzeme ile kaplanması ve ayrıca Moiré yüzeyleri kullanılması ile değişik kovuk yapılarının tasarımını ve deneysel olarak gösterimini içermektedir. İlk metotda hareketli yüzey plazmonlarının optik özellikleri, çift periyoda sahip yüzeylerin yüksek dielektrik sabitli malzemelerle kaplanması sayesinde kontrol edilebilmiş ve bu kontrol plazmon kovuklarının gerçekleştirilmesini sağlamıştır. Bu yapıların oluşumu, deneysel olarak plazmonun yayılımının engellendiği dalga boyu aralığında, hareket edebilen yeni bir yüzey plazmon modunun ölçülmesiyle gösterilmiştir.

Yüzey plazmonlarının yüzeye dik doğrultuda yerelleşmiş olmalarının yanısıra, bu yapılar sayesinde plazmonların hareket yönünde de belirli bölgelerde yerelleşirler. Bu çalışmalara ilaveten, bu çift periyotlu yapıların, çeşitli moleküllerin Raman ve fotoışıma sinyallerinin kuvvetlendirilmesi için de kullanılabilecegi gösterilmiştir. Çalışmalarımızda Raman sinyalinde 10^5 mertebesinde ve fotoışımada ise 30 kat artış gözlenmiştir. Son olarak Moiré yüzeyleri, plazmonlar için yüksek kalite faktörüne sahip kovuk yapıların elde edilmesi için kullanılmıştır. Moiré yüzeylerinde plazmonların yerelleşip ve yavaşlayabilecekleri gösterilmiştir. Moiré yüzeylerinde faz kayması içeren bölgeler kovuk gibi davrandıkları ve birbirine komşu olan kovukların aralarında etkileştiği gözlenmiştir. Moiré yüzeylerinin üzerinde ve plazmon bandının merkezinde hareket hızının $v = 0.44c$ düştüğü ve bandın kenarlarında ise plazmon hızının sıfıra yaklaştığı gözlemlenmiştir. Moiré yüzeylerinde yüzey geometrisinin sinüs fonksiyonu şeklindeki değişiminden dolayı, kovuk yapılarında oluşan saçılma kaybı azalmış ve kalite faktörü 103 civarında ölçülmüştür.

Anahtar sözcükler: Plazmonik, Yüzey plazmon polaritonlar, Çift periyotlu kırınım ağları, Band aralığı, Kovuklar, Moire yüzeyleri.

Acknowledgement

I am indebted to my family for their continuous support and care.

Finally, I dedicate this dissertation to my wife.

Contents

CONTENTS

List of Figures

LIST OF FIGURES

LIST OF FIGURES

LIST OF FIGURES

to my wife

Chapter 1

Introduction

Recent advancements in nano fabrication methodologies allow the design, fabrication and testing of previously proposed quantum mechanical events in the nano-scale leading to new pathways to minimize the sizes of optoelectronic devices. In this regard, nanophotonics is one of the emerging fields investigating light and material interaction in objects engineered at the nanoscale. Photonic band gap structures, ultra high Q photonic cavities [4], ultra fast lasers [5], quantum optical systems [6], biological [7] and chemical sensors [8] have been successfully and extensively demonstrated using dielectric based nanostructured photonic surfaces. In dielectric based optical nanostructures, device sizes are typically restricted by the wavelength of light due to the diffraction limit (Rayleigh criteria, $d \sim \lambda/2$). However, it has recently been shown that metallic structures can overcome this diffraction limit and allow guiding in the sub-wavelength regime by the excitation of surface plasmon polaritons [2, 9-13]. Although the surface plasmon polaritons (SPP) have been known for 50 years (Ritchie, 1957 [14]), this field has started to receive closer attention especially during the last decade. The main reason behind this remarkable interest is the potential application of SPPs in guiding light below the diffraction limit [2]. In analogy with electronics, the word plasmonics was coined by the H.A. Atwater at the beginning of 2000s [1] to cover the science and technology of surface plasmon polaritons and their expanding applications. Plasmonics is thus highly active research area dealing, in the broadest of terms, with light-metal interactions.

Specifically, history of light-metal interactions in the nanoscale, goes back to the beginning of this century when optical anomalies were observed in the reflection spectra of light scattered from periodic metallic structures particularly in one dimensional metallic gratings. This phenomenon was called Woods anomaly [15]. Further studies have proved that SPP plays an essential role in this event. In the following years plasmons have found extensive applications in many areas of science and technology. The contributions from a wide spectrum of scientists ranging from chemistry, biology to physics have made plasmonics a multi disciplinary research field [16].

1.1.   Milestones of Plasmonics

Surface plasmons polaritons can be broadly classified into two types: localized and propagating plasmon polaritons. Localized plasmon polaritons occur as a result of the interaction between light and metallic particles of nanometric dimensions. First observation of this kind of plasmons took place in the fourth century A.D. in the now famous Lycurgus cup. This Roman goblet has gold and silver nanoparticles embedded in glass which exhibit remarkable color decorations. This goblet appears in two different colors, green in reflection but red in transmission. Metallic nano-particles inside the glass matrix absorb the green part of the incoming white light and then scatter it to cause the green reflection. The physics behind this mechanism is based on the Mie theory of the light scattering from the spherically shaped particles [1, 16]. By engineering the shape, size and composition, optical properties of these nanoparticles can be widely tuned. There are numerous techniques to obtain nanoparticles. Among many possibilities, solution-phase synthesis technique has become a versatile chemical method to fabricate these types of particles [16]. On the other hand, e-beam lithography allows fabrication of similar metallic arrays of nanosized

particles [3]. The shape of the particles dramatically alters the scattering spectrum and full range of the visible spectrum can be spanned.

In 1974s, dramatic enhancement of the Raman signal was observed when the molecules were placed on rough metallic surfaces [17]. During the following years, this event was associated with presence of plasmonic excitations [18]. Further studies showed that metallic nanoparticles can support a plasmonic resonance at specific wavelengths in a wide spectral range and enhance the Raman signal [19]. This enhancement leads to the spectroscopy of single molecules using properly designed nanoparticles, previously impossible. Following the nanotechnological progress, especially the developments in self assembly of nanostructures; many kinds of nanoparticles have been widely used in sensing and medical diagnostic applications [20]. To cite a few, recently, Halas et.al. injected plasmonic particles into cancerous tissue and succeeded in killing the cancerous tissue by illuminating the tissue with light at the absorption resonance of the metallic nanoparticles [21]. In a totally different field, metallic nanoparticles were used in lighting technologies as well. In 2004, Scherer et.al [22], improved the light intensity emitted from GaN based LEDs by a factor of 14, by coating these devices with dense gold and silver particle arrays. In summary, metallic nanoparticles exhibit remarkable optical properties due to localized plasmons and can find numerous applications in many walks of daily life.

Alternatively, an important part of plasmonic research concerns the properties of propagating surface plasmons. The most important discovery in this field was performed by Thomas Ebbessen etal in 1998 [23]. They observed that metallic surfaces textured with nanoholes exhibit extraordinary optical transmission. The intensity ratio of the transmitted light to the incoming light was measured to be much greater than that is allowed by the percentage area of the nanoholes.

In general, if the size of the hole is less than the wavelength of the illuminated light, transmitted fields become near field. However, on metallic surfaces, light can transmit through these nanoholes. Initial approaches to explain this observation were based on the existence of plasmonic excitations. Further investigations clarified this point and it was concluded that not only the plasmons but also the diffracted evanescent waves contribute to this extra ordinary transmission [24]. This experiment has extensively stimulated the research on the plasmonics due to the possibilities of creating a new generation of photonic devices. In 2000s, the researchers at California Institute of Technology (Atwater Group) demonstrated that light can be guided at the sub-wavelength scale using a linear chain of gold dots [25, 26]. Furthermore, Miyazaki et al. was able to squeeze a photon having a wavelength of 600 nm into a 55 nm wide cavity geometry [27]. It must be mentioned that all of these systems suffered from the absorption losses of the metal. New approaches, such as metal-dielectric-metal sandwich configurations and long range plasmonic waveguides decreased the loss and improved the propagation length of propagating plasmons up to mm range [28-30]. The analogues of photonic crystal geometries demonstrated in dielectric materials with forbidden photonic band gaps, have also been applied to plasmonic systems [31]. Plasmonic crystals show similar suppression behavior for propagating plasmons on these metallic surfaces. Another significant contribution of propagating plasmons in the field of optics is the use of plasmonic structures for sub-diffraction imaging [11, 13]. In 2005, Fang et.al was able to image features with sizes as small as 89 nm using light with 365 nm wavelength. In total, these experiments have drawn the main framework of the plasmonics research and have opened the way for new approaches for sub-wavelength optics. Thus it has been possible to guide light below the diffraction limit in very thin metallic layers (10-50 nm thick) and with very small effective wavelengths. These

approaches allow squeezing light down to dimensions as small as 10 % of its original wavelength in vacuum.

1.2. Aim and Organization of the Thesis

Studying the confinement of fundamental excitations in cavities has always been rich in physics and technology. A good example is the confinement of light in cavities which gave us the laser. Confinement of electrons in quantum wells has been a proving ground for quantum mechanics as well leading to the diode laser, the quantum cascade laser and the quantum well infrared detector. Phonon and exciton confinement has vastly increased our understanding of solids, semiconductors in particular. While under closer scrutiny for sometime, propagating surface plasmons are only recently being considered for confinement. We have explored plasmonic confinement through the use of selective loading of grating structures as well as through the use of Moiré surfaces. This approach makes the use of holographic lithography possible for cavity fabrication, eliminating the need for extensive e-beam writing. We observe the localization of the plasmons in both cases as obtained in numerical simulations of the structures through time dependent finite difference algorithms. We, furthermore, observe and explain coupling between cavities and explain it through a tight binding model so well applied to coupled resonant optical waveguides. Consequences of plasmonic confinement could in principle be very interesting. A plasmonic analog to lasers has not yet been demonstrated. We suggest that the result obtained in this thesis is the first step in this direction.

In this thesis, we demonstrate the two kinds of plasmonic band gap cavities. We also report on applications of these structures to surface enhanced Raman scattering experiments.

After a brief introduction in Chapter 1, Chapter 2 summarizes the optical properties of metals. Since, plasmons are collective oscillations of electrons in metals, it is important to understand their behavior and how the fundamental constants arising from this is obtained. The main models for dielectric constants of metals are explained and the optical constants of real metals are discussed.

In Chapter 3, we summarize the fundamentals of surface plasmon polaritons. We underline the basic principles of plasmons polariton formation and propagation of surface plasmon polaritons of flat and periodic surfaces.

In Chapter 4, we focus on the plasmonic band gap structure based on biharmonic grating structures. In this chapter, we give the theoretical background and the results of simulations, fabrication techniques and systematic experimental studies for fabrication of these plasmonic cavities.

In Chapter 5, we report on the application of biharmonic gratings. We have demonstrated that these plasmonic band gap surfaces can strongly modify the emitted Raman signal of molecules placed on it.

Chapter 6 has been dedicated to the second kind of plasmonic cavity geometry. We used a Moiré surface to localize the propagating surface plasmons. This cavity structure exhibits a

coupled plasmonic cavity behavior and due to the suppressed radiation, losses yield a relatively high quality factors.

In Chapter 7, we finally conclude with a summary of achievements.

Chapter 2

Optical Properties of Metals

2.1. Drude and Lorentz Model for Dielectric Constants of Metals

In order to understand the properties of plasmons it is important to understand the electronic and optical properties of metals. Optical properties of materials depend on the how electrons within the materials respond to the applied electric field. The simple characteristics of electrons can be modeled within the harmonic oscillation of electrons under driving applied fields [33]. The equation of motion including the damping term can be written as

$$m\ddot{x} + m\Gamma\dot{x} + m\omega_0^2 x = -eE \tag{2.1}$$

m, is the mass of the electron, Γ is the damping term due to the energy loses, ω_0 is the resonance frequency of the oscillation, and E, is the electric field applied to the system. The solution can be easily derived in frequency domain for monochromatic light;

$$(-m\omega^2 - i\omega m\Gamma + m\omega_0^2)x(\omega) = -eE(\omega) \tag{2.2}$$

and the dielectric function can be written as [33]

$$P = N\langle p \rangle = N\hat{\alpha}\langle E_{loc} \rangle = \chi_e E$$
$$\hat{\varepsilon} = 1 + 4\pi N\hat{\alpha}$$
$$\varepsilon = \varepsilon_1 + i\varepsilon_2, \tag{2.3}$$
$$\varepsilon_1 = 1 + \frac{\omega^2_p(\omega_0^2 - \omega^2)}{(\omega_0^2 - \omega^2)^2 + \Gamma^2\omega^2},$$
$$\varepsilon_2 = \frac{\omega^2_p \Gamma \omega}{(\omega_0^2 - \omega^2)^2 + \Gamma^2\omega^2}$$

$\hat{\alpha}$ is the atomic polarizability, χ_e is the susceptibility, ω_p is the plasma frequency and defined as $\omega_p^2 = 4\pi Ne^2/m$, where N is the number of atoms in unit volume [33]. This model of the dielectric function is known as classical Lorentz oscillator model. In dielectric materials, valance band is filled with electrons and these electrons shows a bound behavior and can not move freely. However in metals, valance band is partially occupied and conduction electrons are unbounded. There is no restoring force and the resonance frequency is almost zero. The model of dielectric function of metal can be extended from Lorentz model. The new model is known as the Drude model. In this model, dielectric function becomes [33]

$$\varepsilon = 1 - \frac{\omega^2_p}{\omega^2 + i\Gamma^2\omega} = \varepsilon_1 + i\varepsilon_2$$
$$\varepsilon_1 = 1 - \frac{\omega^2_p}{\omega^2 + \Gamma^2}, \tag{2.4}$$
$$\varepsilon_2 = \frac{\omega^2_p \Gamma}{\omega(\omega^2 + \Gamma^2)}$$

For instance, the optical parameters for silver are; $\Gamma \equiv 0.06eV$ and $\omega_p \hbar = 7.9eV$ and the corresponding relative permittivity is $\varepsilon(800nm) \sim -25 + 1i$ at the wavelength of 800nm. Seen in Fig.2.1 are the real and imaginary pats of the dielectric functions of metal and dielectric materials calculated from Drude and Lorentz model, for comparison dielectric material has the same parameters with resonance absorption around $\omega_0 \hbar = 2eV$. When we look at the frequency dependence, real part of the dielectric function indicates a significant behavior around plasma frequency. Below the plasma frequency $\varepsilon_1 < 0$ and above, it becomes positive $\varepsilon_1 > 0$. However, this important value is not notable in the graph for ε_2. The second important characteristic is that dielectric materials respond like a metal for frequencies higher than the resonance frequency.
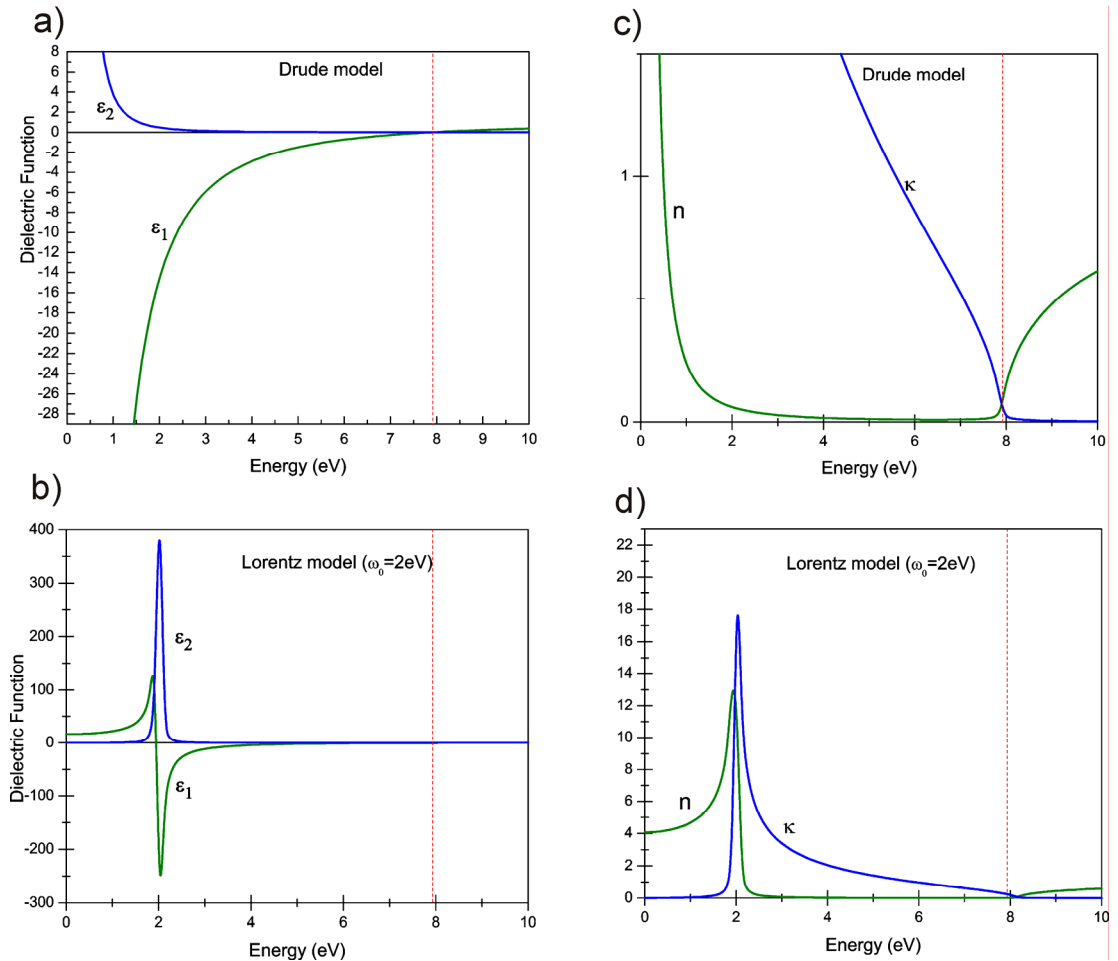
Figure 2.1   (a) real (ε_1) and (b) imaginary (ε_2) parts of the dielectric functions. (c) Refractive index and (d) absorption coefficients, calculated from Drude and Lorentz models, respectively.

Other important optical parameters that can be calculated from these dielectric functions;

$$n(\omega) = \sqrt{\frac{1}{2}(\sqrt{(\varepsilon_1^2 + \varepsilon_2^2)} + \varepsilon_1)}$$

$$\kappa(\omega) = \sqrt{\frac{1}{2}(\sqrt{(\varepsilon_1^2 + \varepsilon_2^2)} - \varepsilon_1)}$$

(2.5)

$n(\omega)$ and $\kappa(\omega)$ are the optical refractive index and the absorption coefficient of the materials. Figure.2.1.c and Fig.2.1.d show the calculated values for previously used Drude and Lorentz models. In metals, the refractive index approaches to zero when frequency is close to plasma frequency. Effective wavelength of light in a material can be defined as $\lambda_{eff} = \lambda_0/n$. This means that as the frequency of the light approaches to the plasma frequency, wavelength of the light extend through the metal. This extended field creates a completely in-phase collective oscillation of the free electrons. This oscillation is known as plasma oscillation. Additionally, absorption coefficient of the metal approaches zero around the plasma frequency and for higher frequencies metals acts as a dielectric and becomes transparent. This optical response is observed as a drop in reflectance spectrum. This drop in reflection suppresses a part of the wavelength spectrum and determines the color of the metal.

2.2. Optical Constants of Real Metals

Although noble metals (Au, Ag, and Cu) have similar plasma frequencies corresponding to plasmon energies around 8eV ($\approx$155nm), they appear in different colors. Simple Drude model is not adequate in explaining why gold is yellow but silver is colorless. Real metals have aspects of both Drude and Lorentz models [33]. The electronic configurations of

silver and the gold are $[Kr]4d^{10}5s^1$ and $[Xe]4f^{14}5d^{10}6s^1$, respectively. In the case of silver, the electron in $5s^1$ yields the metallic behavior and the energy of 4d orbital is close to that of 5s orbital and they lie just below the Fermi level. At optical wavelengths, it is possible to excite the interband transitions of bound 4d orbital electrons to just above the Fermi level. This situation completely changes the dielectric response of real metals. For instance, in silver, 4d electrons have an additional resonance around $\omega_0 \hbar = (E_F - E_D) \sim 3.9eV$ [33]. These polarized electrons make the real part of the dielectric function zero at this interband resonance frequency. A new plasma oscillation is observed at this resonance frequency. Figure.2.2 shows the experimental dielectric constants and the reflectivity of silver. Plasma frequency of silver is shifted to $\omega_0 \hbar = 3.9eV$ and a sudden drop appears in the reflection spectrum. Similarly gold has a resonance at $\omega_0 \hbar \sim 2.5eV$ [33] and this makes gold appear as yellow. In measurements and simulation of plasmonic devices, these optical constants are extremely important to understand the plasmon physics. Simple Drude model is useful in simulations for the infra-red wavelength range. However, at visible wavelengths, especially below 500nm, the mixed model and accurate experimental data for dielectric constants should be considered. On the other hand, for very low frequencies especially in the microwave regime, the real part of the metal dielectric constant converges towards $-\infty$. For these frequencies, metals can be considered as a perfect conductor thus, they cannot support any bound states on the surface making it impossible to excite surface plasmon modes in the microwave range. Real plasmonic modes have been observed in the THz frequency regime. However, periodically structured surfaces can show surface plasmon-like modes. These surface modes are called as spoof plasmonic modes [34, 35]. These surface modes may also be confused with surface plasmon polaritons. Plasmonic research

in these extreme frequencies (UV and microwave) requires care to clarify the correct plasmonic excitations.
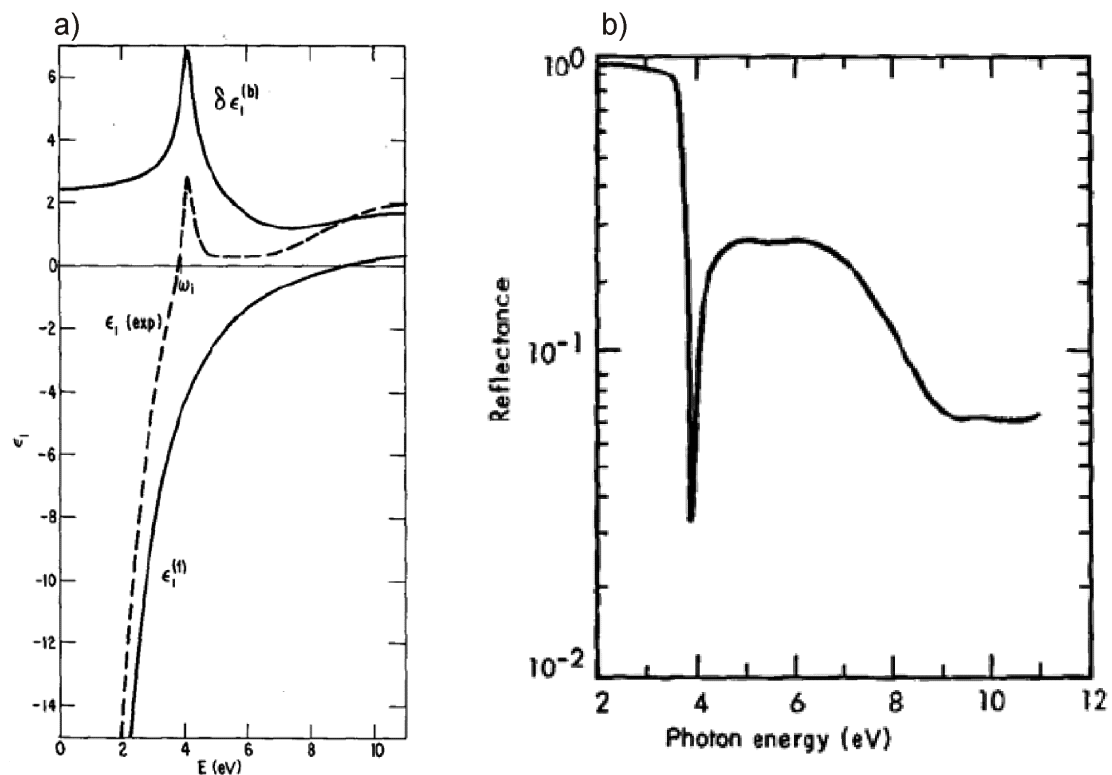
Figure 2.2 (a) Experimental and theoretical (Drude model) dielectric constants and, (b) Reflectance spectrum of silver. (Adapted from Ref.[33])

Chapter 3

Fundamentals of Surface Plasmon Polaritons

3.1. Field Distributions of Surface Plasmon Polaritons

Surface plasmon polaritons (SPP) are dipole-carrying electromagnetic waves generated by coupling of collective oscillation of free electrons and photons. Metals can supply the free electrons to form an electron sea [36]. In the previous chapter, we described the dielectric responses of the metals and dielectrics. Below the plasma frequency, metal-dielectric interface exhibit positive and negative permittivities. The significance of this difference in permittivities can be seen by considering the field distributions on metal-dielectric interface. Positive and negative charges on a metal sustain the electric fields. Figure 3.1 shows the TM polarized case of field distributions of propagating SPPs. Electric fields originate on the positive charges and terminate on the negative ones. $E_{\parallel}$ and $H_{\parallel}$ are continuous on the boundary. Additionally, a fast response of the free electrons leads to continuity of the displacement field ($\nabla.D_{\perp} = \rho = 0$). The charges in a metal having a high conductivity have very short relaxation times of the order of $\tau \sim 10^{-18} s$. Oscillation frequency of optical fields is much slower than the relaxation time of the electrons. Consequently, we can set the charge density to zero ($\rho \sim 0$). The electric field supported

by the charges changes sign across the interface. Displacement field can be written as $D_\perp = \varepsilon E_\perp$ and the continuity of displacement field requires a boundary having negative and positive permittivities. This is the reason why the SPP occurs on the metal-dielectric interface. In field configurations, H fields are always parallel to the metallic surface while the electric fields have both perpendicular and parallel components in metal and dielectric medium. In the dielectric side, the ratio of the field amplitudes can be written as $E_\perp \big/ E_\parallel = \sqrt{\dfrac{\varepsilon_m}{\varepsilon_d}}$ and in the metallic side as $E_\perp \big/ E_\parallel = -\sqrt{\dfrac{\varepsilon_d}{\varepsilon_m}}$. If the frequency is far away from the plasma frequency, electric fields in the metallic side become dominantly transverse, this transverse field oscillates the electron longitudinally in forward and backward directions parallel to the metallic surface.
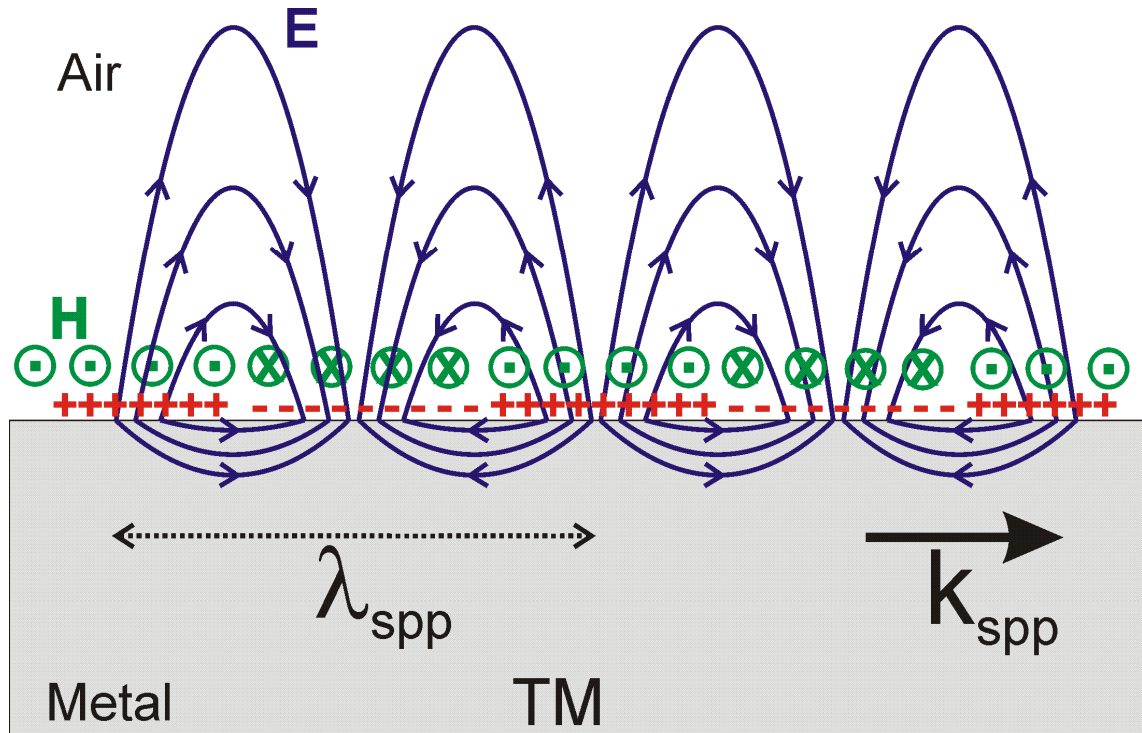
Figure 3.1 TM case, electric and magnetic fields distribution of SPP propagating on metal dielectric interface.

It is a well known property that SPP can be excited only with TM polarized electromagnetic fields. The reason for this can be clarified by plotting the TE case for SPP field distributions. Figure 3.2 shows the impossible field distribution for the TE case. Due to the absence of magnetic monopoles, H fields should be divergence free. Additionally, at the interface $E_\parallel$ and $H_\parallel$ should also be continuous. Both of these constraints contradict at the boundary that $H_\parallel$ fields have opposite directions at the metal dielectric interface. This opposite field distributions inhibit the existence of TE polarized SPP on metal-dielectric interface. A more detailed explanation of this behavior is given in Ref. [37]
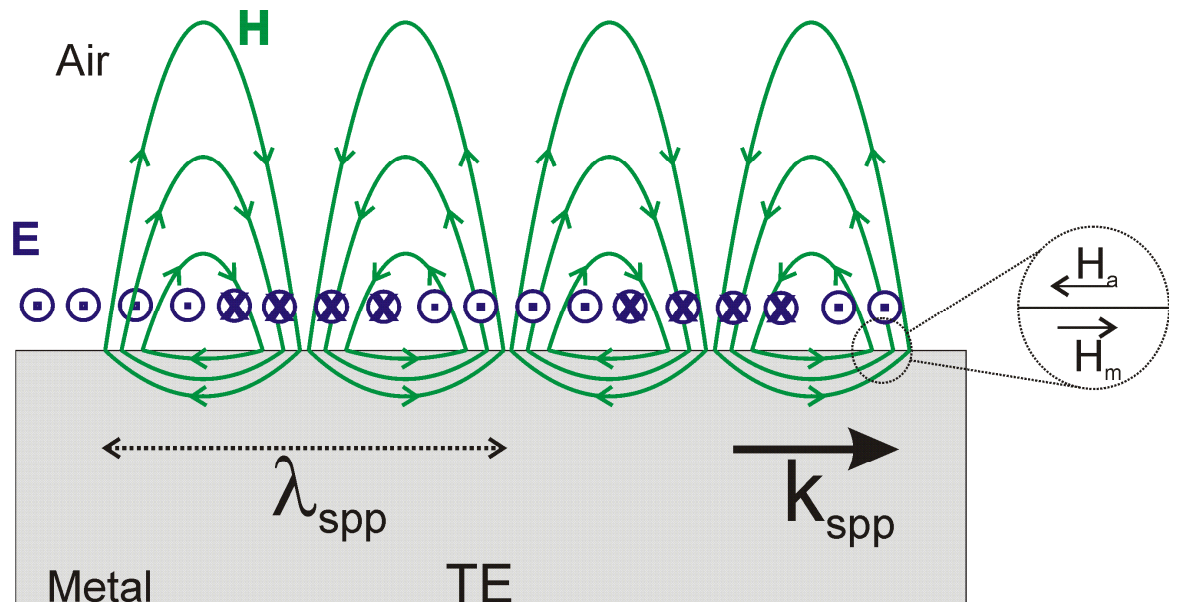
Figure 3.2 TE case, electric and magnetic fields distribution of SPP propagating on metal dielectric interface. Opposite directions of $H_\parallel$ fields show the physical impossibility of TE case SPP.

3.2. Dispersion of Surface Plasmon Polaritons

The physics of the SPPs can be understood by extracting the dispersion relation. The solution of the Maxwell equation with proper boundary conditions, on metal-dielectric interface reveals the dispersion of the propagating SPP. The calculation was given systematically in Ref. [36]. Briefly, by applying the continuity of tangential E and D fields, the well-known dispersion curve, giving the relation between the energy and the momentum of SPP can be calculated as

$$k_{spp} = \frac{\omega}{c}\sqrt{\frac{\varepsilon_m \varepsilon_d}{\varepsilon_m + \varepsilon_d}}$$

(3.1)

where, k_{spp} is the wavenumber of the propagating SPP, ε_m and ε_d are the relative permittivities of metal and dielectric and ω, c are frequency and the speed of the light. In our case, for simplicity, we use air as a surrounding dielectric medium with a permittivity of $\varepsilon_d = 1$. The dielectric response of the metal plays a crucial role in the dispersion relation of SPP. The metal shows a dispersive dielectric response and similarly this dispersive behavior appears in SPP dispersion. Figure 3.3 shows the dispersion curve for SPP at the silver-air interface. As described in the previous chapter, plasma frequency of silver is observed at $\omega_p \hbar = 3.9\,\text{eV}$ in contrast with what is expected from the Drude model. A new resonant frequency value is clearly observed in the dispersion if we set the dielectric constant of air as $\varepsilon_d = 1$, where the dispersion relation becomes $k_{spp} = \frac{\omega}{c}\sqrt{\frac{\varepsilon_m}{\varepsilon_m + 1}}$ and a singularity is obtained when $\varepsilon_m(\omega_R) = -1$. From the Drude model, this resonance frequency can be calculated as $\omega_R = \frac{\omega_p}{\sqrt{2}}$. However, in contrast with the Drude model, due to the additional contribution of the d orbital electrons in silver, the resonance frequency which makes $\varepsilon_m(\omega_R) = -1$ shifts to $\omega_R \hbar \sim 3.7\,\text{eV}$. Below this resonance, bound SPP modes exist. This bound mode asymptotically converges to the resonance frequency for larger wavevectors and for shorter ones, SPP mode converges to the light line.
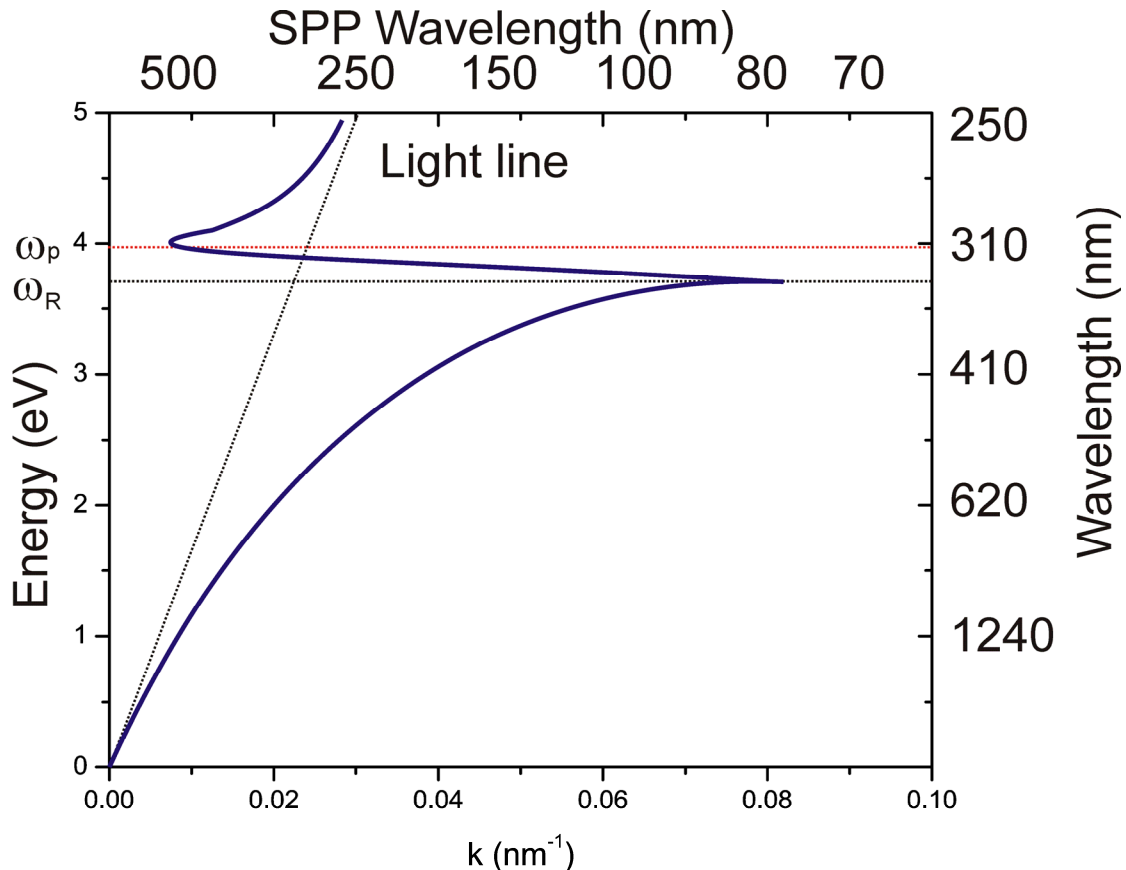
Figure 3.3 The dispersion relation of Surface Plasmon Polaritons propagating on metal dielectric interface.

In the transparency region, for frequencies higher than the plasma frequency $(\omega > \omega_p)$, radiative bulk plasmon modes are observed. In this region, the metal acts as a dielectric and has $\varepsilon_m > 0$. Again, using the free electron model, the dispersion of this radiative mode can be written as $\omega^2 = \omega_p^2 + k^2 c^2$. In this thesis, we focus on the bound SPP modes rather than the radiative ones. According to free electron model, the frequency band between the resonance frequency and plasma frequency should act as a natural band gap region and can

not allow propagation of plasmons. However, experimentally it is possible to excite this quasi-bound plasmon mode in this region where they exhibit negative phase velocity.

Focusing on the bound SPP modes, the dispersion relation can be simplified as

$$k_{spp} = \frac{\omega}{c}(1 + \frac{1}{2|\varepsilon_{m1}|} + i\frac{\varepsilon_{m2}}{2(\varepsilon_{m1})^2})$$ if $\varepsilon_{m2} \ll |\varepsilon_{m1}|$ and $|\varepsilon_{m1}| \gg 1$. Similarly, we can define the

effective refractive index of SPP as

$$n_{spp} = 1 + \frac{1}{2|\varepsilon_{m1}|} + i\frac{\varepsilon_{m2}}{2(\varepsilon_{m1})^2} \qquad (3.2)$$

It should be noted that real part of the refractive index ($n_r = 1 + \frac{1}{2|\varepsilon_{m1}|}$) is always larger

than 1. This refractive index results in the SPP bound mode. Due to its bound nature, the corresponding momentum ($p = \hbar k_{spp}$) becomes higher than that of the free space propagating light.

3.3. Wavelength of Surface Plasmon Polaritons

Effective wavelength of the plasmon is related to the oscillation period of the electron density wave. Wavelength of SPP can be written in terms of its wavevector (momentum) as $\lambda_{spp} = 2\pi/k_{spp}$ and results in

$$\lambda_{spp} = \lambda_0\sqrt{\frac{\varepsilon_m + \varepsilon_d}{\varepsilon_m \varepsilon_d}} \qquad (3.3)$$

The wavelength of SPP shrinks dramatically as the ε_m approaches to -1. Top scale of the Fig. 3.1 shows the plasmonic wavelength. We can see that, for example, if the SPP can be excited with light having a wavelength around 360 nm, then, the wavelength of the plasmon becomes 100 nm. This shrinking in wavelength is important for sub-wavelength

optics. Using plasmonic waveguides, it is possible to guide the light at the sub-wavelength scale. On the other hand, SPP fields can penetrate into both dielectric and metal surroundings. The penetration depths of the electric field into both the top cladding and bottom cladding can be found by solving for the perpendicular wavevector components. Both wavevectors are imaginary and penetration depths can be written as [38]

$$\delta_d = \frac{1}{k_0}\left|\frac{\varepsilon_{m1} + \varepsilon_d}{\varepsilon_d^2}\right|^{\frac{1}{2}}$$

$$\delta_m = \frac{1}{k_0}\left|\frac{\varepsilon_{m1} + \varepsilon_d}{\varepsilon_m^2}\right|^{\frac{1}{2}}$$

(3.4)

δ_d and δ_m show different behavior as a function of wavelength. Field penetration depth in dielectric side decrease as the wavelength approaches to the resonance frequency. This means, for these wavelengths plasmon gets localized in vertical direction about the metal dielectric interface while its wavelength is shrinking. However, in contrast with the dielectric side, penetration dept into metal starts to increase as the wavelength approaches resonance. Furthermore, the optical loss of the metal at the resonance frequency is rather high and plasmonic resonance becomes overdamped. The imaginary part of the refractive index, ($n_{im} = \frac{\varepsilon_{m2}}{2(\varepsilon_{m1})^2}$), determines the propagation length of the SPP. Thus, in the visible part of the spectrum, imaginary part of the optical constant of metals is relatively high and this restricts the propagation length within few dozens of micrometers. For frequencies close to the resonance, propagation length is around a few micrometers. There is a trade-off between the localization of SPP in the vicinity of the surface and the propagation length. This obstacle can only be solved by using a gain medium instead of a dielectric environment. Recently, there have been proposals in this regard [39].

3.4. Excitation of Surface Plasmon Polaritons

Dispersion relation clearly demonstrates the bound nature of SPPs. We have also seen that dispersion curve of SPPs lies below the light line. Basically this means that there is a momentum mismatch between the SPP and free space propagating light. This mismatch inhibits the excitation of SPPs on flat metallic surfaces. However, resonant coupling can only occur when the momentum of the incident light matches with the momentum of the SPP. There are three common methods to overcome this momentum mismatch [36]. Figure 3.4 schematically represent these excitation mechanisms. In the first method, surface plasmon resonance can be achieved under conditions of attenuated total reflection (ATR). The idea for the use of an ATR goes back to the work of Otto and Kretschmann. In this configuration, a prism having high refractive index enhances the momentum of the incident light when the sample is illuminated from the prism side. By scanning the angle of incidence (α), the resonant excitation can be achieved. The optimum excitation condition strongly depends on the metal thickness. Illuminated light is partially reflected from prism-metal interface and transmitted light pass trough the thin metallic film and excite the SPP by polarizing the charges. SPP can also be reradiated with a phase change. The partially reflected light and the (antiphase) [36] reradiated field interfere with each other. Thus, in order to minimize reflection, proper design of the metal thickness is required. The resonance condition can be formulated as

$$k_{spp} = n_{eff}k_o = n_p k_0 Sin(\alpha) \tag{3.5}$$

a)

$k_{spp}=n_{eff}2\pi/\lambda$

α

n_p

$k_0=2\pi/\lambda$

b)

Λ_{gr}

c)
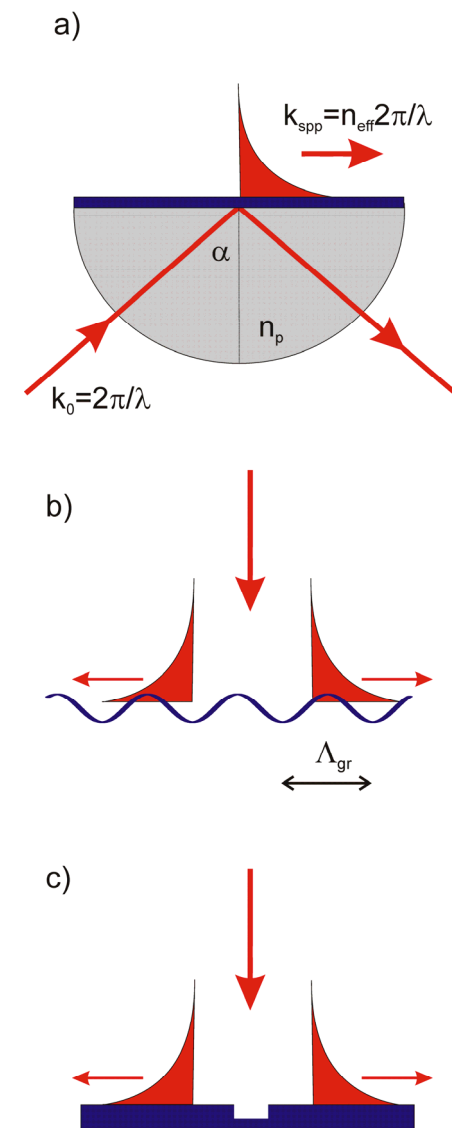
Figure 3.4 Three different commonly used SPP excitation mechanisms (a) Prism coupler, (b) Grating coupler and the (c) Trench scatterer.

The second method utilizes a grating fabricated on the surface of the metal that acts as a coupler. Figure 3.4.b shows the grating coupler configuration. Due to the periodic corrugation on the metal surface, the momentum of the light is increased. This property of the metal grating allows exciting the SPP from both sides of the grating. In the grating case, metal thickness does not significantly affect the SPP excitation strength. Similarly, partially reflected light and re-radiated anti-phase SPP, should interfere destructively for optimum SPP excitation and resulting in a reduction in reflectivity. This excitation condition is governed by the well known Bragg equation;

$$k_{spp} = n_{eff}k_o = k_0 Sin(\alpha) + m\frac{2\pi}{\Lambda}$$
(3.6)

where the Λ is the periodicity of the grating structure and m is the diffraction order. Due to the periodic surface and the wave nature of light, periodic medium can add or subtract the momentum in in-plane direction. By changing the incidence angle and tuning the wavelength of the light and monitoring the reflected light, all available SPP modes on the metallic surface can be measured. The third excitation scheme is based on the sub-wavelength scatterer (Fig. 3.4c). Mainly, nanoscale trenches on metallic surfaces can excite the SPP mode. In our experiments, we have only used prism and grating coupler techniques to excite the SPP modes.

3.5. Propagation of Surface Plasmon Polaritons on a Periodic Surface

So far we have investigated the excitation and dispersion of a SPP on flat metallic surfaces. In this section, we will extend the theory for SPP propagation on periodically textured metallic surfaces. Furthermore, we will analyze the dispersion diagrams of propagating SPPs on different metallic surfaces.
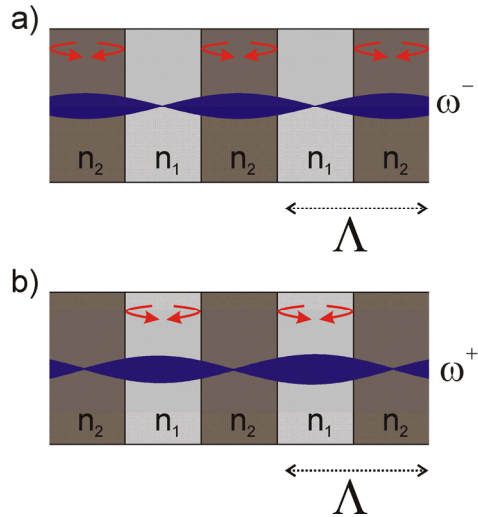
Figure 3.5 Schematic representations of field localizations associated with (a) lower and (b) higher energies localized at higher and lover refractive index regions, respectively.

In analogy with the condensed matter physics, periodic dielectric medium can alter the propagation of light passing through this medium. The high index medium for the photon corresponds to low potential energy for the electrons in a periodic electronic potential formed by the atomic lattice. These periodic dielectric structures are known as photonic crystals [40]. Figure 3.5 represents the one dimensional periodic structure. It consists of periodically stacked low (n_1) and high refractive (n_2) index mediums. When the light launched into this structure, it will be scattered at each boundary. Due to the resonance, if the periodicity is half of the effective wavelength of the light, forward propagating light can be scattered into backward direction. Then, both forward and the backward propagating light interfere and form a standing wave. Figure 3.5 shows available configurations these standing waves form. Using symmetry, it can be shown that reflected waves become in-phase just at the center of each region. Consecutively, lower energy configuration (ω_-)

modes are localized in high index region and otherwise, high energy configuration (ω_+) placed at the low refractive index side. The wavelengths coinciding between these energies ($\omega_+ < \omega < \omega_-$) destructively interfere and can not propagate through the structure. This suppression band is known as photonic band gap [40].

Similarly, for a plasmonic system, rather than refractive index contrast, corrugations on metallic surfaces act as a scattering center. If the corrugations form a periodic structure, same band gap formation can take place. Figure 3.6 indicates the electric field distributions of the SPPs associated with lower and higher energy configurations at the band edges of the gap. In the plasmonic case, different localization sides on the grating result in an energy difference. It is seen that for low energy configuration, free charges are placed on the troughs of the grating and this leads a field that localizes on the peaks. Otherwise, charges localizing on the peaks make the field localize on the troughs [41]. The distortion in electric fields lines increases the energy of the mode. In Fig. 3.6, the second field distribution has more distributed field shape and its energy higher than the first one. Besides the difference in their associated energy, localized modes exhibit a different penetration profile. The lower energy configuration has more confined behavior than the higher one. In the next chapter, this property will be used and allow us to control the width of the band gap.

a)

E

ω^-

λ_{spp} Λ_{gr}

b)

E

ω^+

λ_{spp} Λ_{gr}
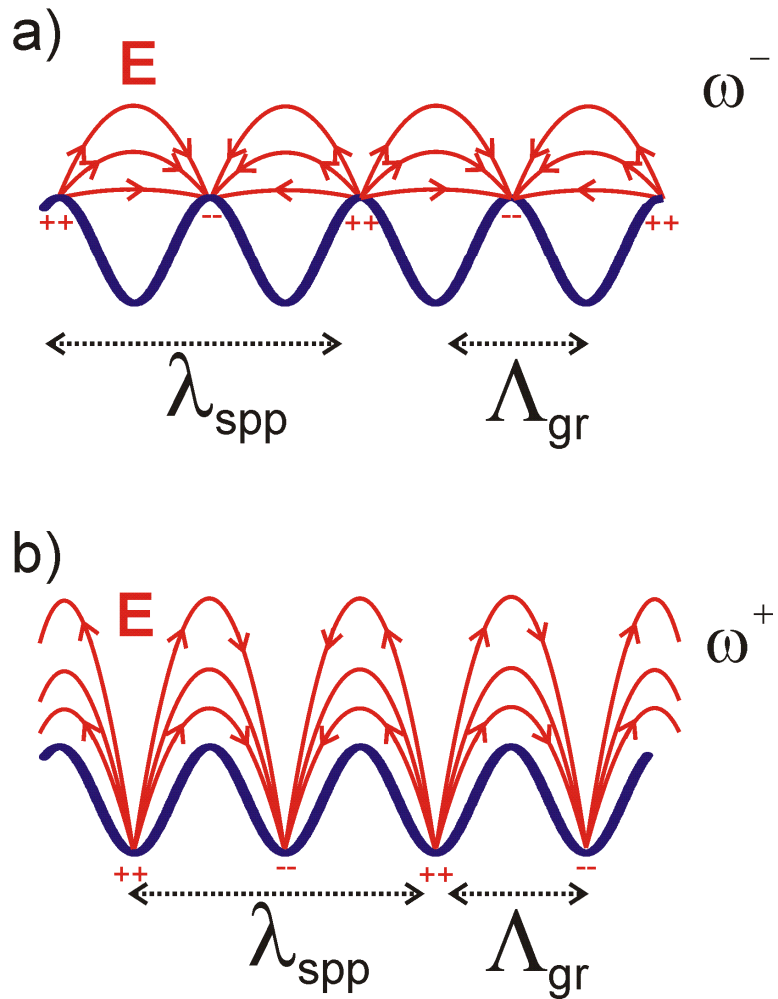
Figure 3.6 Schematic representations of the electric field distributions of SPPs localized on the grating. (a) Lower energy configuration localizes on the troughs and (b) higher energy configuration localizes on the peaks.
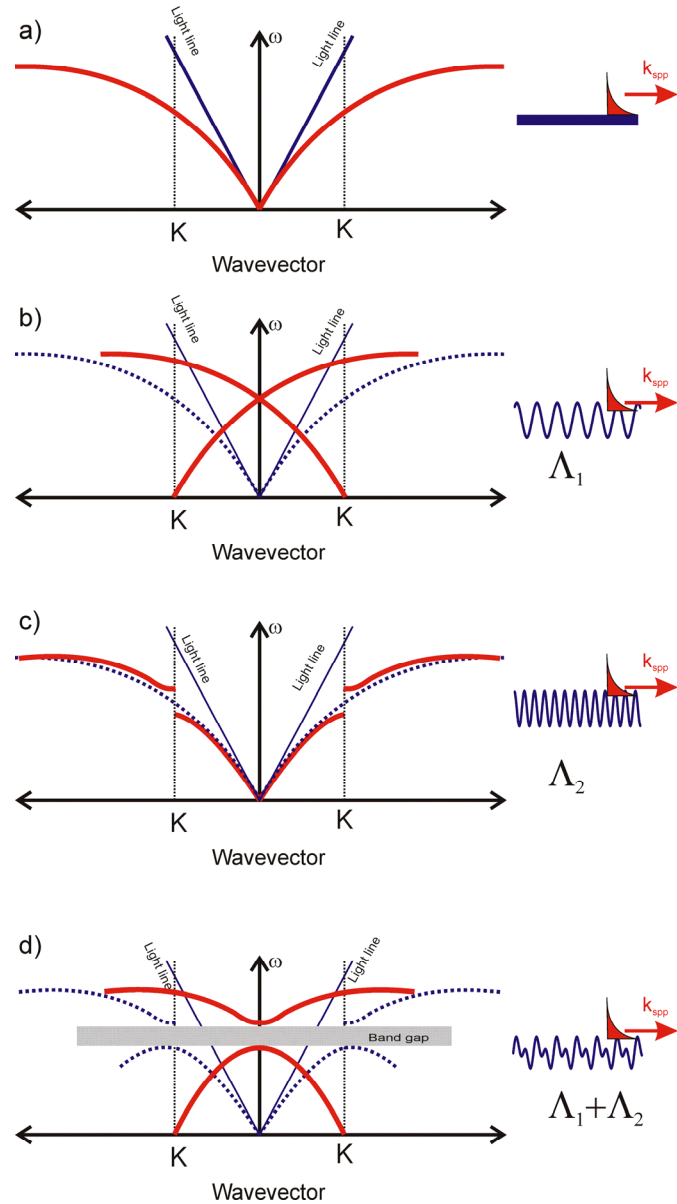
Figure 3.7 Dispersion curves of SPPs on (a) flat metal surface, (b) on uniform grating Λ_1 (c) on uniform grating having a periodicity Λ_2 (d) on biharmonic grating

3.6. Dispersion Diagrams of SPP on Periodic Surfaces

Although, free space propagating light and the excited bound plasmon, have the same frequency, their dispersion curves can not be matched, due to the difference in their momentum. Dispersion of bound plasmonic modes always lies below the light line. Figure 3.7.a shows the dispersions of the light and the bound SPP mode. As described in previous sections, this mismatch inhibits the SPP excitation on flat metal surface. However, as seen in Fig.3.7.b, periodic grating surface can shift the dispersion above the light line. This makes possible the excitation of SPP through direct illumination with the light. In plane momentum vector can be tuned by changing the incidence angle and allows acquiring the resonance excitation. By scanning the wavelength and the incidence angle all band structure can be mapped. In normal incidence, crossing point is observed in dispersion. This means that there is degeneracy in the energy of forward and backward propagating SPPs. Both can be excited simultaneously. Furthermore, if the periodicity of the grating is half of the effective wavelength of SPP, band gap formation will take place at the edges of the first Brillion zone. Figure 3.7.c schematically represents the dispersion having a plasmonic band gap. Similarly, due to same momentum mismatch problem, it is impossible to construct the dispersion. Applying the same grating coupling methodology, one can move the dispersion within the light line. Construction of dispersion curve having a band gap requires both a grating component for excitation and band gap formation. Figure 3.7.d indicates the resulting dispersion curve. At normal incidence one can observe energy splitting instead of the crossing degeneracy point [41]. In the following chapters, all experiments and band structure measurement methods are based on these excitations.

Chapter 4

Plasmonic Band Gap Cavities on Biharmonic Gratings

In this chapter, the formation of plasmonic band gap cavities in infrared and visible wavelength range are experimentally demonstrated. The cavity structure is based on a biharmonic metallic grating with selective high dielectric loading. A uniform metallic grating structure enables strong surface plasmon polariton (SPP) excitation and a superimposed second harmonic component forms a band gap for the propagating SPPs. We show that a high dielectric superstructure can perturb the optical properties of SPPs dramatically and enable the control of the plasmonic band gap structure. Selective patterning of the high index superstructure results in an index contrast in and outside the patterned region that forms a cavity. This allows us to excite the SPPs that localize inside the cavity at specific wavelengths satisfying the cavity resonance condition. Experimentally, we observe the formation of a localized state in the band gap and measure

the dispersion diagram. Quality factors as high as 37 have been observed in the infrared wavelength.

4.1. Introduction

Collective oscillations of electrons coupled to light form SPP's [36] that are confined to metal- dielectric interfaces and propagate along the interface with decaying intensity due to complex dielectric function of metals. Their small mode volume and sensitivity to the effective index makes SPP's attractive for many applications [2]. In addition to already proven biosensing applications [42], other diverse possibilities such as increased luminescence efficiency from nanocrystal emitters [43], nanolithography [44] and nanophotonic applications [38, 45, 46] are being studied. In contrast with propagating modes and associated with bound electron plasmas, localized SPP's on small metal particles or voids [47-50] also attract much attention due to enhanced fields [51] particularly for applications such as surface enhanced Raman scattering [52, 53]. Such localized modes are bound on curved surfaces of metal particles characterized by size and shape dependent discrete states with various frequencies. The possibility of localizing propagating modes have lately also been attracting interest [32, 54, 55]. Theoretical approaches show that propagating SPPs can also be localized through the use of a properly designed cavity that supports these modes [56]. Very recently, progress in the theoretical analysis of such cavities has been confirmed with the demonstration of a grating based cavity using Bragg mirrors [32]. Unfortunately, this approach just allows mapping the electric field distribution through the cavity. Direct observation of cavity formation from plasmonic band structure has still been lacking. Cavities for propagating SPP modes can also be constructed through selective index loading of grating based SPP systems. In this approach, part of the grating system corresponding to the cavity is left untouched while an

extra layer of high dielectric material is deposited onto the grating outside the cavity. The induced effective index contrast between the cavity and its surroundings results in the localization of propagating modes [40] much like those that are supported by Bragg mirrors [32, 56-58]. Additionaly, our approach allows extracting extensive information on the band structure of the cavity and the dispersion of the cavity state in a very simple way for both preparation and characterization of the cavity structure.

The design of such cavities starts by taking into account the dispersion of SPP's on a metallic surface. Dispersion of SPPs is determined by the dielectric functions of the metal and dielectric environment and results in the SPP wave number being greater than that of propagating light in the same dielectric medium [36]. Use of a grating coupler is one way to compensate for the momentum mismatch between the light and the SPP and excite SPP's on metallic surfaces [59]. In this work, we employ grating structures to couple to the plasmons as well as to form the plasmonic band gap [60]. The cavity is formed by selective index loading of the grating structures.
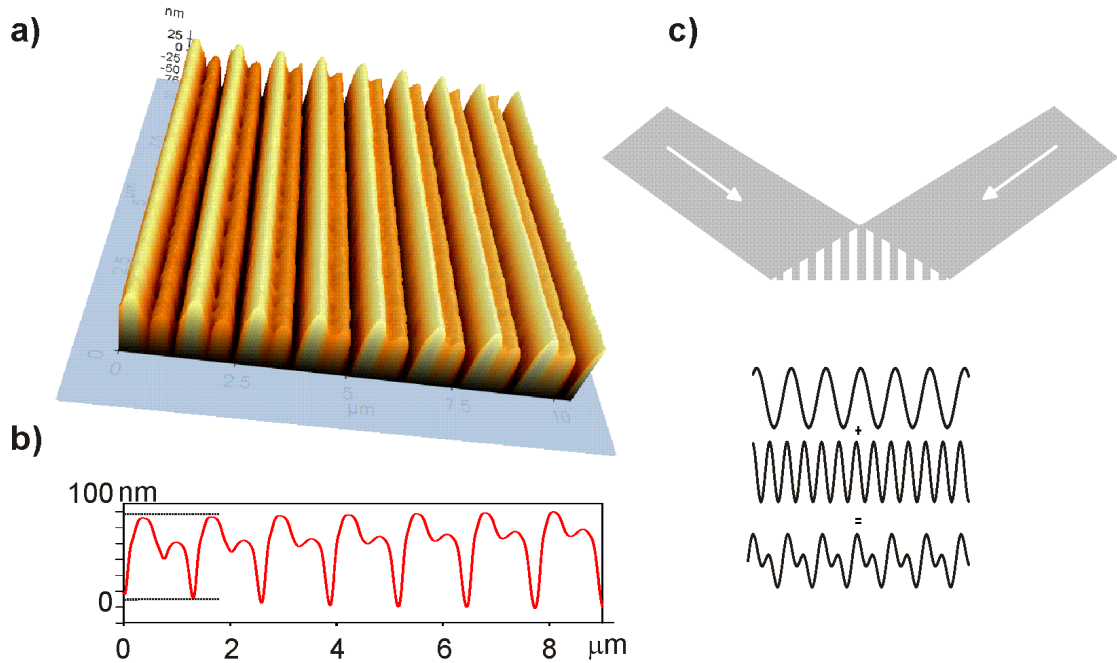
Figure 4.1 (a) 2D AFM image of biharmonic metallic surface. First periodicity is designed to couple free space light to SPP's. Second one generates backscattering for propagating SPP's and opens up a photonic band gap. (b) Line profile of AFM image. (c) Schematics of double exposure method for grating fabrication.

4.2. Fabrication of Cavity Structures

A uniform grating with fixed periodicity was used to couple light to the plasmons. In order to form a plasmonic band gap structure at the wavelength of excitation, additional periodicity needs to be used. This leads to the formation of a biharmonic grating structure. Figure 4.1.a shows the AFM image of the biharmonic grating structure used for plasmonic excitation [41, 61]. Gratings with two different periods were successively recorded on a photosensitive polymer (AZ1505) by holographic double exposure interference lithography

(Fig. 4.1.c). Figure 4.1.b shows line profile of the biharmonic grating, including two different grating components with periods of Λ_1=1330 nm and Λ_2=665nm. Once developed, the structure has been transferred on photocurable epoxy (OG 146 Epoxy Technology) by nanoimprint technique with a soft elastomeric mold [62]. The replication procedure can be summarized as follows; biharmonic master grating template was prepared using interference lithography, which is used to make the elastomeric stamp. Liquid PDMS (Sylgard 184, Dow Corning) was poured on the master grating and cured at 75 °C for 2 h. After the curing procedure, elastomeric stamp was peeled off from the master grating and placed on the pre-polymer (OG146) coated wafer. Pre-polymer was cured using UV light exposure. Finally, the elastomeric stamp was mechanically removed from the wafer. The photocurable epoxy is chemically inert for the latter optical lithography processes. 50 nm-thick silver (Ag) film was evaporated on cured epoxy to form a metallic periodic structure. The long periodicity (Λ_1) allows coupling between the incoming photon and the trapped SPP's propagating in forward and backward directions. The SPP coupling is observed at a specific wavelength and the incidence angle, satisfying the following equation;

$$k_{spp} = n_{eff}k_0 = k_0 sin(\alpha) \pm m\frac{2\pi}{\Lambda} \tag{4.1}$$

k_{spp} and n_{eff} are the wave number and effective refractive index of the SPP's, k_0, α and Λ are the wave number of the incident photon, angle of incidence and periodicity of the grating structure, respectively. Dispersion curve of SPP on a flat metal surface lies outside the light line and unable to measure. However, the long periodicity changes the dispersion and moves the dispersion curve within the light line thus allows the measurement of dispersion around normal incidence. Measurement of the coupling wavelength and angle reveals the dispersion of the SPP's. Dispersion curves of SPP modes are constructed by scanning the incidence angle and measuring the wavelength dependent reflectivity from the

surface. In order to construct the band structure, the reflectivity was measured as follows; collimated white light generated by an FTIR spectrometer (TENSOR 37) was directed on to the sample. Back reflected beam from the sample was collected using beam a splitter and detected with an InGaAs photo detector. Reflectivity measurements were taken with different incidence angles from which two dimensional reflectivity maps were constructed. Finite set of measurements were interpolated using linear interpolation algorithm with MATLAB.
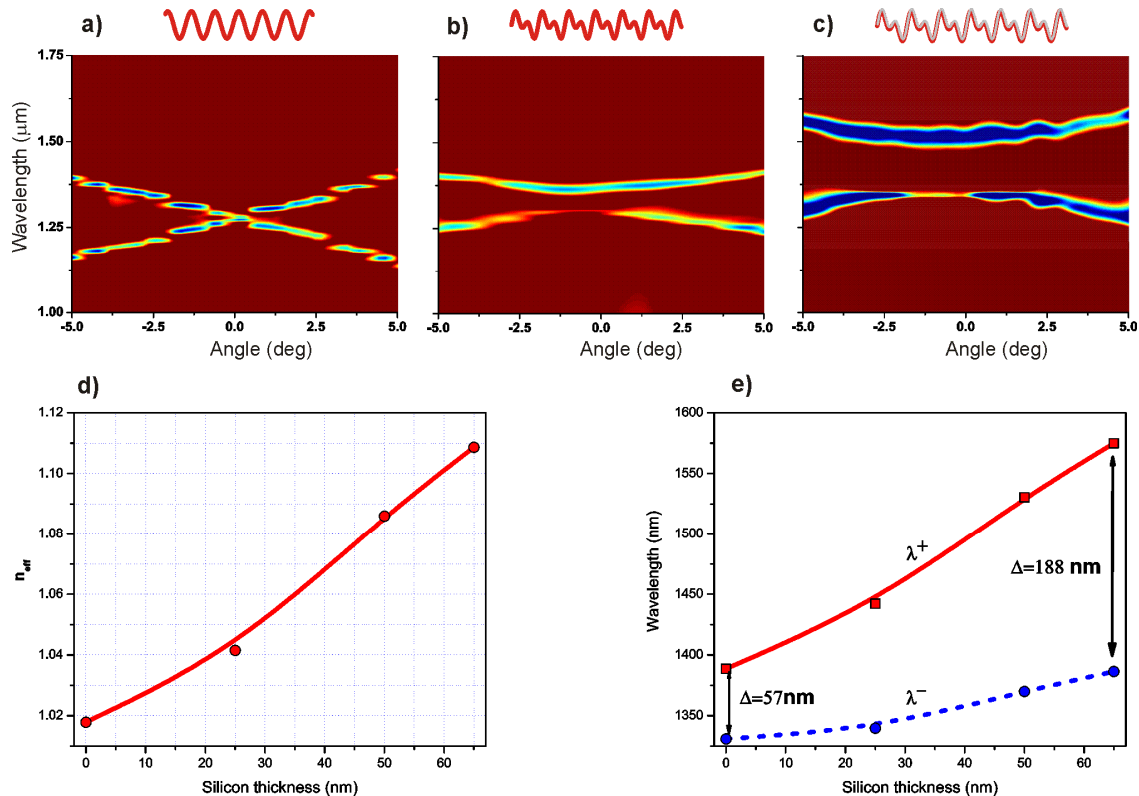
Figure 4.2 Experimental dispersion curves of SPP's on (a) uniform, (b) biharmonic, (c) silicon-loaded biharmonic metallic surface and (d) effective refractive indices as a function of silicon thickness. (e) Wavelengths of upper and lower bands λ^+ and λ^- as functions of silicon thickness

Figure 4.2 shows the wavelength dependent reflectivity map of different grating structures as a function of incidence angle. Corresponding grating structures are schematically shown on top of each dispersion curve. In Fig. 4.2.a, each band represents the forward and backward propagating SPP's on a uniform (Λ_1=1330 nm) grating structure. Uniform grating compensates for the momentum mismatch and acts as a coupler. Second order diffraction from the uniform grating is very weak; hence SPP's on these types of periodic structures do

not show a gap in the dispersion at the excitation wavelength. We note that the mini gaps seen in the dispersion curve are due to discreteness of measurements, sharp resonances do not allow for interpolation. As described in previous chapter, addition of the second periodicity onto the first one results in a biharmonic structure and creates a backscattering on the propagating SPP's and leads to the formation of standing waves on the biharmonic grating structure. Since the SPP's localized on peaks and troughs of the periodic structure have different energies, a band gap opens up between these lower and higher energy bands, denoted by λ^+ (or ω^-) and λ^-(or ω^+) respectively. As seen in Fig. 4.2.b, the biharmonic structure (Λ_1=1330 nm + Λ_2=665 nm) leads to a band gap with a width of Δ=57 nm around normal incidence. Controlling the properties of the surface of this structure is critical for fine tuning the characteristics of the band gap. We observe that depositing a thin layer of silicon with full coverage changes the effective indices of the SPP's significantly without perturbing the SPP excitation.
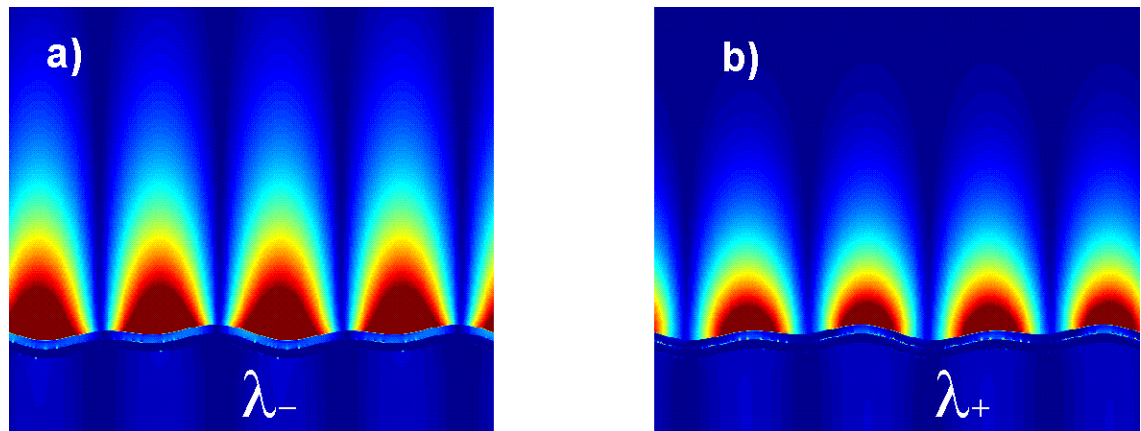
Figure 4.3 FDTD simulation results for electric field distributions localized on biharmonic metallic structure illuminated with wavelengths of λ- and λ+.

It is well known that field distributions of λ^+ and λ^- branches of SPP's at the band edges show different confinement behavior [41]. Figure 4.3 shows the FDTD simulation results for electric field distributions on a biharmonic metallic grating structure illuminated with the wavelength of λ- and λ+ respectively. λ- localizes on the troughs, while λ+ localizes on the peaks of the periodic structure. It seen that λ^+ and λ^- show different confinement behavior. Field of λ^+ (Fig. 4.3.b) becomes more confined to the interface than that of λ^- (Fig. 4.3.a). This extra confinement makes λ^+ more sensitive to surface properties. Thus, loading the biharmonic metallic structure with high dielectric material should increase the energy difference between λ^+ and λ^- bands which would directly affect the width of the band gap. This reasoning has been tested with incremental loading of a metallic biharmonic grating structure with silicon (Si). Figure 4.2c shows the dispersion diagram of a biharmonic structure uniformly coated with 50 nm-thick Si. The Si coating increases the central wavelength and widens the band gap. We systematically changed the Si thickness and measured the dispersion. Figure 4.2d summarizes these results. There is an increase of effective indices of SPP's as the silicon thickness increases. From Eq. 4.1 for normal incidence illumination, effective index of SPP's can be written as $n_{eff} = \dfrac{\lambda}{\Lambda}$. Figure 4.2.d shows the measured effective indices, n_{eff} of SPP's. The effective index can be tuned from $n_{eff} = 1.02$ to $n_{eff} = 1.11$. Finally, as seen from Fig. 4.2.e, deposition of a Si layer increases the width of the band gap up to $\Delta = 188$ nm. Thus, we demonstrate the ability to systematically control not only the effective index but also the width of the band gap.

On grating structures, forward and backward propagating SPP's having a wavelength in the band gap interfere destructively. However, local perturbation of the effective index can lead to an extra phase change in the propagating waves and can result in constructive

interference at a specific wavelength which is a cavity mode. Hence, the capability to control the local effective index of SPP's enables the fabrication of plasmonic cavities on grating structures. Therefore, in the presence of a cavity, SPP's with a previously forbidden wavelength can propagate when the following the resonance condition is met [32, 63]:

$$L \cdot \Delta n = (2m+1)\frac{\lambda}{4}$$
(4.2)

where L is the cavity length, Δn is the index perturbation and λ is the central wavelength of the band gap. We, therefore, expect to observe a cavity mode at the central wavelength.

If the cavities are close to each other, coupling takes place. Figure 4.5 shows the finite difference simulation of these coupled cavities and shows the plasmon hopping through cavities. A mask with a number of cavities with the same geometry separated by 100 μm to prevent a coupling between cavities on both sides in an area of 10mmx10mm was used to lithographically define the cavity structure on the biharmonic metal surface and a 65 nm-thick Si was deposited on surface outside the cavity regions. This approach is much simpler than the physical removal of periodicity in a grating. Furthermore, this approach makes the use of holographic lithography possible for cavity fabrication, eliminating the need for extensive e-beam writing. Figure 4.4.a is a schematic representation of the cavity geometry. From Fig. 4.2.d, the effective refractive indices of SPP's in silicon-coated and uncoated regions, are n_0=1.017 and n_1=1.108 respectively. The corresponding effective index difference is Δn=0.091 and the resulting cavity length for the central wavelength of λ=1.479 μm is L= 4.1 μm.

a)

n_1 n_0 n_1

L

Silicon
Metal

b)
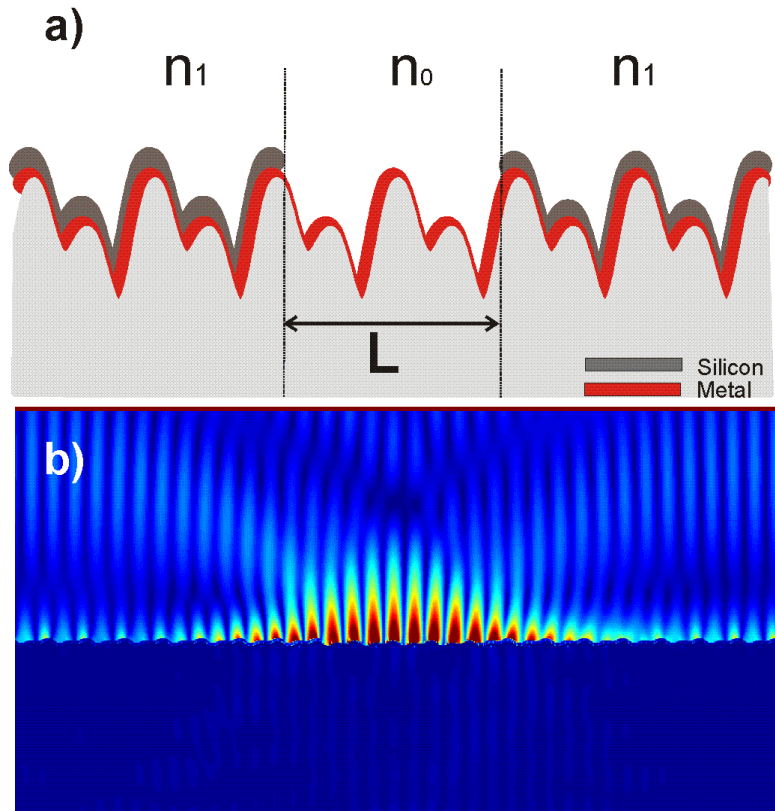
Figure 4.4 (a) Schematic representation of the plasmonic cavity structure. (b) FDTD simulation of electric field distribution in a cavity illuminated with the cavity mode.

We performed finite difference time domain (FDTD) simulations to verify the cavity formation. Figure 4.4.b shows the simulation result of electric field intensity ($|E^2|$). It is seen that propagating SPP's form a standing wave inside the cavity region. This localization depends strongly on cavity size. According to the results of the simulation, optimum cavity length was found be around 5.5μm which is slightly larger than that obtained from equation 2 which is 4.1μm. The difference between experiment and

simulation results from the small difference between refractive index of the evaporated Si and that assumed for the simulation. To clarify the cavity behavior, we measured the dispersion diagram. Figure 4.6.a represents the dispersion diagram of the biharmonic grating structure without the cavity and Fig. 4.6.b shows the same structure with the cavity. An additional absorption peak appears in the band gap region. Red colored band represents the localized cavity mode. To increase the contrast in the dispersion diagram, color scale was normalized to R= 80 % and the diffraction background was subtracted from the reflection spectrum. This state shows a non-dispersive property. The center of the absorption doesn't change as a function of incidence angle as would be expected from a localized state [49]. Figure 4.6.c and Fig. 4.6.d shows the normal incidence wavelength dependent reflectivity. In Fig. 4.6.c, two clear absorption peaks correspond to λ^- and λ^+ at the band edges. Red arrow in Fig. 4.6.d shows additional absorption peak corresponding to cavity mode. The decrement in the reflected intensity below the 1.3µm is due to the diffraction from the grating structure. Experimentally, we observe the cavity state for a 4.5µm cavity length. The quality factor of the cavity defined as $Q = (\Delta\lambda_0/ \lambda_0)$ can be calculated from the reflectivity spectrum. From Fig. 4.6.d, full width at half maximum of the cavity mode is approximately $\Delta\lambda_0 \approx 40$ nm and the corresponding quality factor is $Q = 37$. This quality factor is relatively low for plasmonic cavities as compared with photonic crystal cavities. The overall quality factor can be described as [56]

$$\frac{1}{Q} = \frac{1}{Q_{abs}} + \frac{1}{Q_{rad}} \qquad (4.3)$$

where Q_{abs} and Q_{rad} are the radiative and absorptive quality factors respectively. Q_{abs} is dominated by the metallic loss in plasmonic cavities and Q_{rad} by out-of-plane radiative

losses. Gratings having a larger period component in the cavity region of the biharmonic grating can lead to significant radiative losses. The improvement in quality factor can be achieved by removing the grating structure inside the cavity region. Furthermore, abrupt change of the localized mode profile in the cavity region is the other radiative loss source. Gently modifying the grating amplitude around the cavity may also suppress the radiation losses [4]. Gong et.al [56] proposed the theoretical limit at low temperatures for the quality factor in the case of plasmonic cavities made using Bragg reflectors as 1000. However, experimental quality factors measured on cavities made of Bragg mirrors has been reported at best as 45 [32].
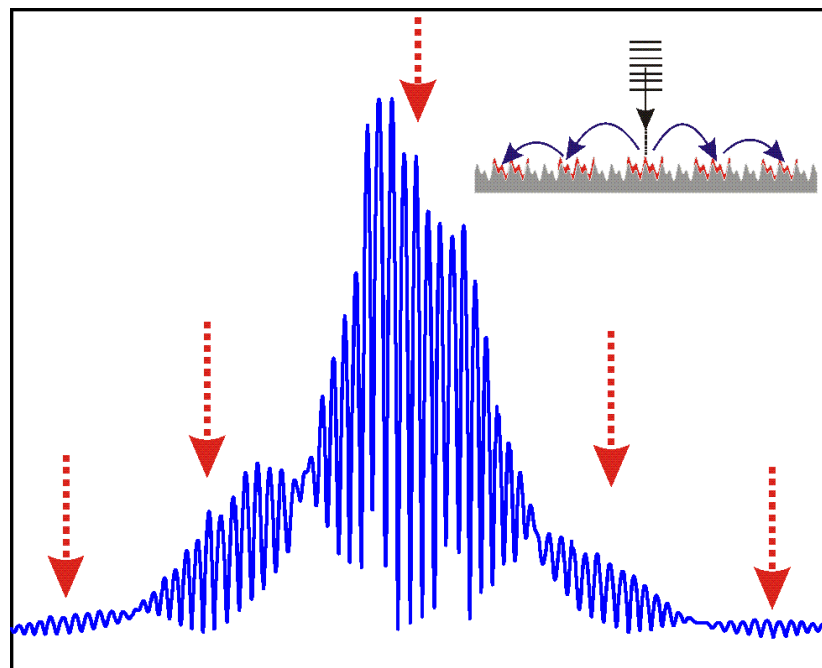
Figure 4.5 FDTD simulation results for plasmon hopping through cavities.
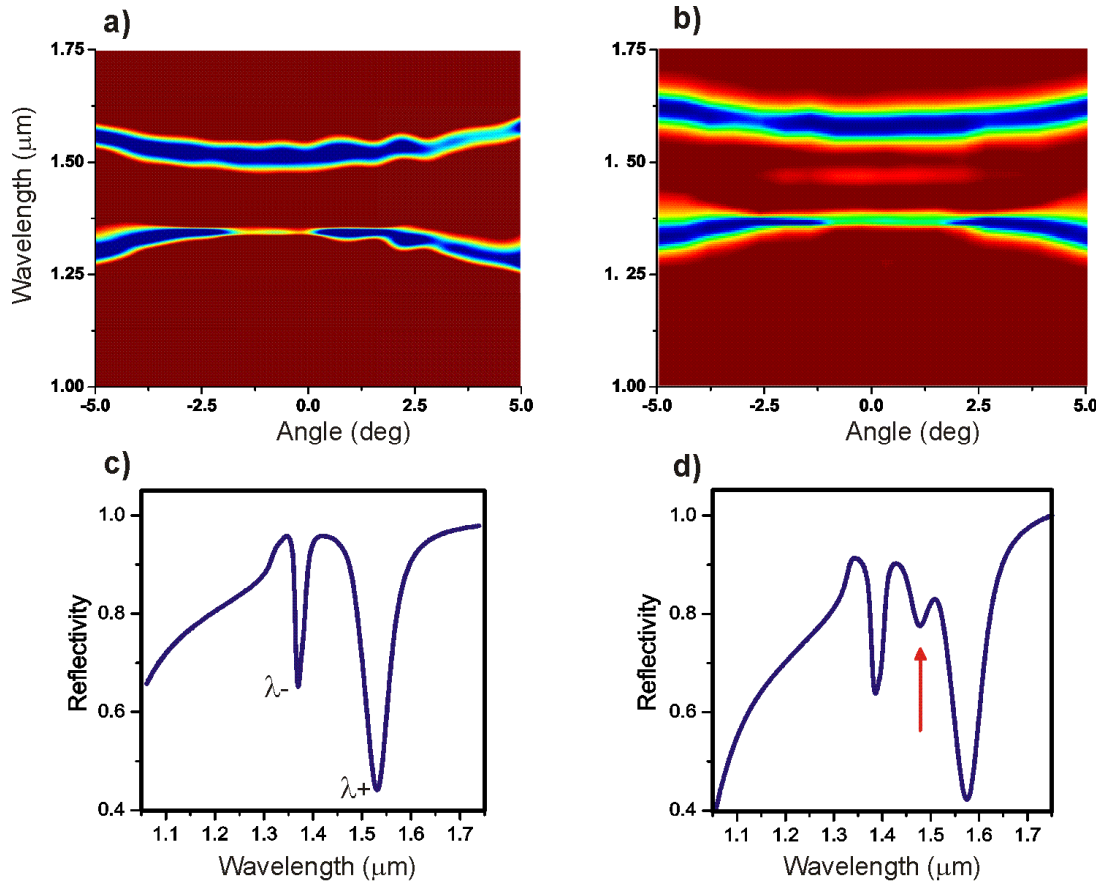
Figure 4.6 Experimental dispersion curves of SPP's on a biharmonic structure a, without a cavity b, with a cavity, and c, d, normal incidence reflectivity spectrum for a, and b, respectively.

We have systematically studied the formation of plasmonic band gap cavities using numerical calculations. Shown in Fig. 4.7 are the FDTD simulation results of reflectivity on different grating structures. Fig. 4.7.a shows the normal incidence wavelength dependent reflectivity of a uniform metallic grating having a periodicity of Λ_1=1330nm. Clear absorption peak corresponds to plasmonic resonance. Si loading onto the uniform

metallic structure increases the effective refractive index of propagating SPP. This increase in refractive index makes plasmonic resonance shift towards higher wavelengths. Figure 4.7.b shows the shifted plasmonic resonance absorption on silicon loaded uniform metallic grating structures. Second order diffraction from the uniform metallic structure is weak and cannot create a band gap. As seen in Fig. 4.7.c superimposing the second grating creates the band gap. Figure 4.7.c shows the reflectivity of biharmonic (Λ_1=1330nm+ Λ_2=665nm) metallic grating structure. Two resonance peaks correspond to λ^- and λ^+, respectively. A narrow band gap becomes apparent when the second harmonic component (Λ_2=665nm) is superimposed on the grating structure. However, bare biharmonic grating creates a narrow band gap and silicon loading can widen the width of the plasmonic band gap while increasing the effective refractive index. Figure 4.7.d shows the reflectivity of the biharmonic (Λ_1=1330nm+ Λ_2=665nm) metallic grating structure uniformly loaded with 50 nm thick Si. Finally, Fig. 4.7.e illustrates the reflectivity of the plasmonic cavity fabricated on silicon loaded biharmonic metallic grating structure. Additional absorption inside the band gap corresponds to cavity resonance.
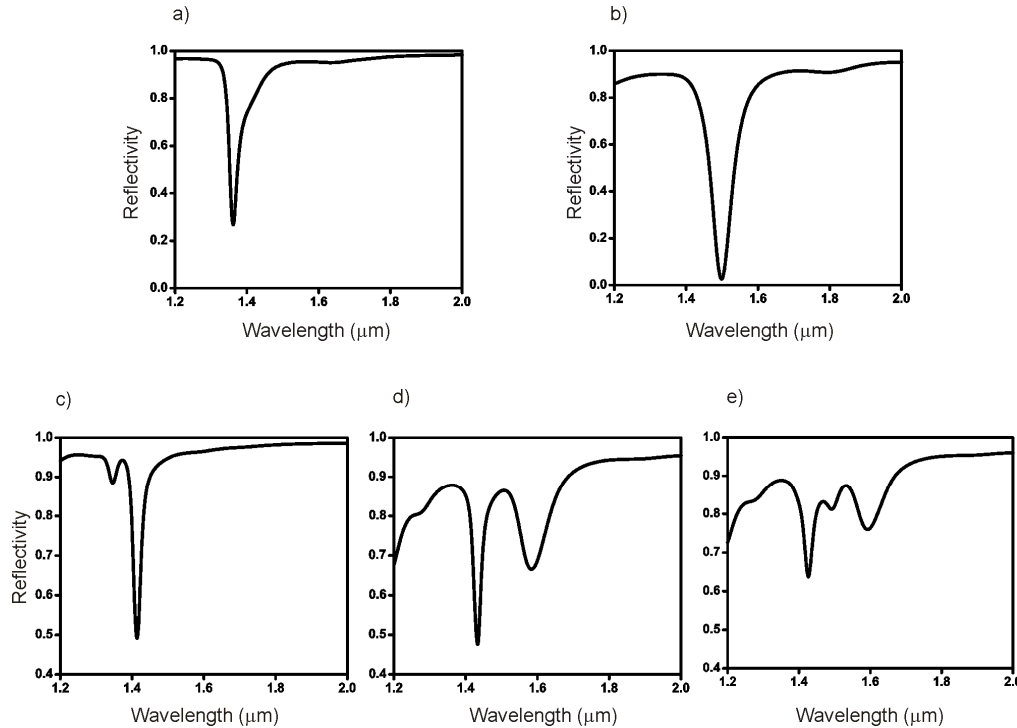
Figure 4.7 FDTM simulation results for reflectivity of the different grating structures. (a) uniform grating (Λ_1=1330nm). (b) 50 nm Si loaded uniform (Λ_1=1330nm). (c) biharmonic metallic grating (Λ_1=1330nm+ Λ_2=665nm). (d) biharmonic (Λ_1=1330nm+ Λ_2=665nm) metallic grating structure uniformly loaded with 50 nm thick Si. (e) plasmonic cavity fabricated on silicon loaded biharmonic metallic grating structure.

Many applications such as displays and light emitting devices require the use of visible part of the spectrum. It would, therefore, be important to demonstrate that the physical principles and fabrication technology is suitable for plasmonic cavity formation in the visible as well. Thus, a plasmonic band gap cavity in the visible regime was designed and fabricated. In this case biharmonic structures consisted of gratings with periods of Λ_1=500 nm and Λ_2=250 nm used for coupling and band gap formation, respectively. A

spectroscopic ellipsometer (WVASE32) was used to measure the reflection in the visible wavelength range. The normal incidence reflectivity of biharmonic structures (Fig. 4.8.a) reveals a wide band gap region in the absence of a silicon layer. To fabricate the cavity, 12 nm-thick Si loading was used for the particular cavity geometry and a 4.5 μm cavity length was defined. A plasmonic cavity was obtained in the visible regime; a cavity state appears inside the band gap as expected (Fig. 4.8.b). The effect of ultra thin layer of Si on the transmission of light is negligible. The effective refractive index of SPP's depends strongly on the thickness of the Si loading and restricts systematic studies at visible wavelengths. Uncertainty in our silicon deposition rates makes it difficult to control the effective indices at the level of the precision required for a more systematic study. Other materials with high dielectric constants may also be used for the same purpose.
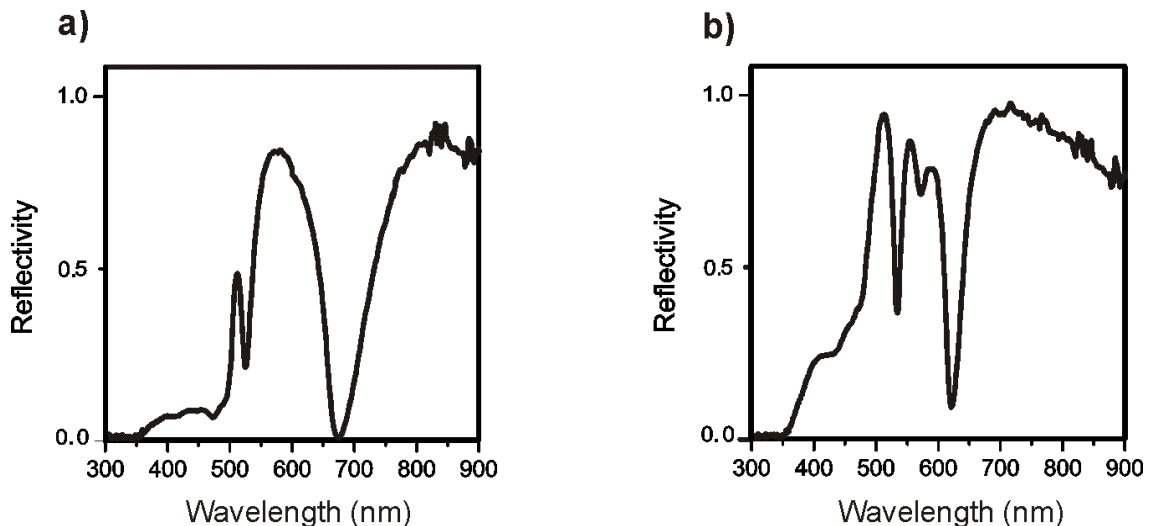
Figure 4.8 Normal incidence reflectivity spectrum of (a) biharmonic and (b) biharmonic with cavity structure in visible wavelength range. A cavity state appears inside the band gap region.

4.3. Conclusion

In conclusion, we have used a grating to couple light to surface plasmons and a second grating superposed onto the first to create a band gap at the excitation wavelength of the first grating. We demonstrated that two superposed grating structures result in a band gap covering the excitation wavelength region. We showed that band gap widths of grating based plasmonic structures can be controlled with the deposition of high dielectric layers. By selective deposition, we have demonstrated the formation of plasmonic cavities through the use of biharmonic grating structures with high dielectric superstructures. We observe cavity modes both in the infrared and the visible part of the spectrum. The approach we use is simple, combining holographic lithography with photolithography to fabricate plasmonic band gap cavities. This approach is suitable for large area applications and it makes plasmonic cavities applicable in examining cavity material interactions.

Chapter 5

Plasmonic Band Gap Structures for Surface-Enhanced Raman Scattering

This chapter was submitted to Optics Express as "Plasmonic Band Gap Structures for Surface-Enhanced Raman Scattering " **Askin Kocabas**, S. Seckin Senlik, Gülay Ertas and Atilla Aydinli, Reproduced (or 'Reproduced in part') with permission from Optical Society of America. Copyright 2008 Optical Society of America.

In this chapter Surface-enhanced Resonance Raman Scattering (SERS) of rhodamine 6G (R6G) adsorbed on biharmonic metallic grating structures was studied. Biharmonic metallic gratings include two different grating components, one acting as a coupler to excite surface plasmon polaritons (SPP), and the other forming a plasmonic band gap for the propagating SPPs. In the vicinity of the band edges, localized surface plasmons are formed. These localized plasmons strongly enhance the scattering efficiency of the Raman signal emitted on the metallic grating surfaces. It was shown that reproducible Raman scattering enhancement factors of over 10^5 can be achieved by fabricating biharmonic SERS templates using soft nano-imprint technique. We have shown that the SERS activities from these templates are tunable as a function of plasmonic resonance conditions. Similar enhancement factors were also measured for directional emission of

photoluminescence. At the wavelengths of the plasmonic absorption peak, directional enhancement by a factor of 30 was deduced for photoluminescence measurements.

5.1. Introduction

Raman spectroscopy is a crucial tool in the analysis of vibrational bonds which reveal the details of the molecular structure. Despite its importance, extremely low cross section of Raman scattering (10-30 cm^2 per molecule) [64] limits its applications in chemical and biological sensing. However, in the vicinity of the noble metal nanoparticles (such as Ag and Au), physical mechanism of the Raman scattering is dramatically altered which results in considerable signal enhancement. This phenomenon is known as Surface Enhanced Raman Scattering (SERS) and the physics behind this enhancement have been extensively studied. The mechanism and applications of SERS have been reported on several review and feature articles [65-69]. It has been shown that localized and propagating plasmons play an essential role in this process. In particular, metallic nanoparticles can absorb light in visible wavelength range and support localized plasmon modes. When the large electric fields generated by these localized modes are at the incoming resonance wavelengths, they lead to large enhancements in the electric field intensity. It should be noted that enhanced Raman signal roughly scales with (Es^4) [51, 70]where Es is the local electric field. This mechanism does not require chemisorption and in general predicts equal enhancements for all molecules with maximum enhancement factors of 10^6-10^7 [51, 52, 67, 71, 72]. In addition, nanoparticles can also increase the out of plane scattering of the Raman signal emitted on their surface at the outgoing resonance wavelengths [64]. It has been previously shown that most favorable condition for SERS is observed when plasmonic resonance absorption lies between the exciting laser and Raman emission wavelengths [20]. With the

help of the metallic nanoparticles, the enhancement factors up to 10^{15} allowing single molecule detection, have been reported [52, 53, 73-76]. Efforts to understand and develop SERS as an analytical tool are dependent on methods for fabricating templates with stable and reproducibly high activities. Typical SERS substrates, textured metallic surfaces such as spherical shapes [77] and pyramidal type voids [78, 79] allow engineering the plasmonic modes to optimize reproducible SERS enhancement. These kinds of structures can support localized plasmonic modes and also localize the propagating surface plasmon inside the voids. On the other hand, rather than voids, metallic grating surfaces can also act as SERS templates [80-83]. Raman signal emitted at the near field of the metallic grating couples to the SPP and is re-radiated into the photon at a specific direction determined by both the wavelength of radiation and the periodicity of the grating. When a Raman active material is deposited on a flat surface, Stokes radiation is emitted into a solid angle of 2π sr. However, on a metal grating surface, Stokes radiation is confined into a much smaller solid angle and results in an enhancement in the measured Raman signal [80]. These types of templates show relatively low enhancement factors (10^4) [80] and enhanced Stokes wavelengths depend on the collection angle as well [82].

In this chapter, we demonstrate that biharmonic metallic grating structures can be used as SERS substrates. Previously, biharmonic grating structures have been used to enhance second harmonic generation [61] and to form plasmonic band gap cavities [84]. Biharmonic surface is made up of a grating with two harmonic components. Higher periodicity couples the incident light into the SPPs while the second shorter grating component forms a plasmonic band gap. Due to the flat dispersion at the vicinity of the band edges, plasmonic density of states is perturbed and effective coupling of emitted signal into the SPP are achieved. We demonstrate the SPP coupled enhancement of PL and

SERS signals. Soft nanoimprint technique is used as a replication tool allowing the fabrication of SERS templates reproducibly.

5.2. Fabrication of Biharmonic Gratings
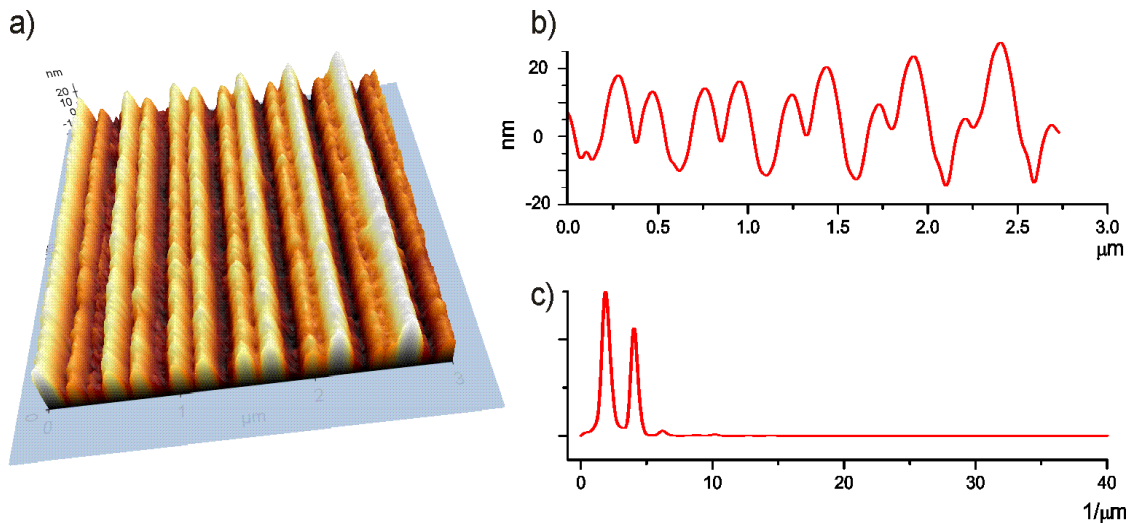
Figure 5.1 (a) 2D AFM image of biharmonic metallic surface includes Λ_1=500 nm and Λ_2=250 nm gratings. First periodicity is designed to excite the SPP's. Second one generates backscattering for propagating SPP's and opens up a photonic band gap. (b) Line profile of AFM image. (c) Power spectrum of AFM image indicating two different harmonic components.

Shown in Fig. 5.1.a is the AFM image of fabricated biharmonic template. Gratings with two different periods were successively recorded on a photosensitive polymer (AZ1505) by holographic double exposure technique. Figure 5.1.b shows line profile of the biharmonic grating, including two different grating components with periodicities of Λ_1=500 nm and Λ_2=250nm. As seen in Fig. 5.1.c, power spectrum clearly shows these two different

superimposed grating components. Once developed, the structure was transferred onto the photo-curable epoxy by soft nano-imprint technique. The replication procedure of the template structure to the polymeric surface is shown schematically in Fig. 5.2. In this procedure, biharmonic master grating template was prepared using interference lithography (Figure 5.2.a), which is used to make the elastomeric stamp. Liquid PDMS (Sylgard 184, Dow Corning) was poured on the master grating (Figure 5.2.b) and cured at 75 °C for 2 h. After the curing procedure, elastomeric stamp was peeled off from the master grating (Figure 5.2.c) and placed on the pre-polymer (OG 146, Epoxy Technology) coated wafer (Figure 5.2.d). Pre-polymer was then cured using UV light exposure (Figure 5.2.e). Finally, the elastomeric stamp was mechanically removed from the wafer (Figure 5.2.f). The photocurable epoxy is chemically inert for the latter processes. 55 nm-thick gold (Au) films were evaporated on cured epoxy to form a metallic periodic structure.
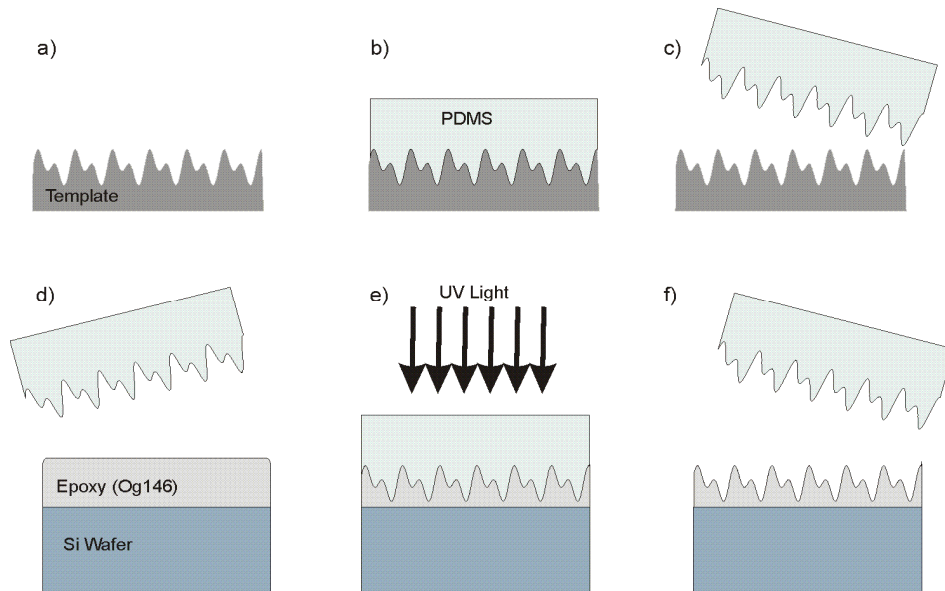
Figure 5.2 Schematic diagram for replication and transfer of the grating structure onto the polymeric surface using the elastomeric stamp (PDMS); (a) Biharmonic master grating template was prepared using interference lithography, (b) the template was prepared by pouring liquid PDMS on the master grating and then cured at 75 °C for 2 h. (c) After the curing procedure, the elastomeric stamp was peeled from the master grating, (d) and then, placed on the pre-polymer (OG146) coated wafer (e) where the pre-polymer was exposed to UV light. (f) Finally, the elastomeric stamp was mechanically removed from the wafer.

Optical reflectivity measurements were carried out using a spectroscopic elipsometer (WVASE32) to investigate the plasmonic excitation on the biharmonic metallic surface. Figure 5.3 shows the normal incidence reflection spectra of as prepared templates for different metallic (Ag and Au) layers. Ag metal shows superior optical response than the Au metal in the visible wavelength range. As seen in Fig. 5.3.a, additional absorption minima occur in TM polarized reflection spectra (electric fields perpendicular to the grating groves). Two different minima correspond to excitation of SPPs at the band edges of the

photonic band gap region. Uniform $\Lambda 1$=500 nm grating component creates coupling between the incoming light and the SPPs propagating in both forward and backward directions. However, superimposed second grating ($\Lambda 2$=250nm) creates back scattering for SPPs. Interfering SPPs form a standing wave having two different localization profiles [41]. As described in previous chapter, λ^- localizes on the troughs, while λ^+ localizes on the peaks of the periodic structure [41]. Similarly, reflectivity measurements were also made for Au deposited biharmonic template. Au metal is highly resistive towards chemical oxidation when compared with Ag metal, therefore, Au coated bihormonic structures were used as SERS substrates throughout this study for SERS measurements. As seen in Fig. 5.3.b, a similar reflectivity spectrum was measured for Au metal. The reason for decrease in reflectivity for both metals below 500 nm is diffraction from the 500 nm grating periodicity. Above 500 nm wavelength scale, diffraction becomes evanescent.
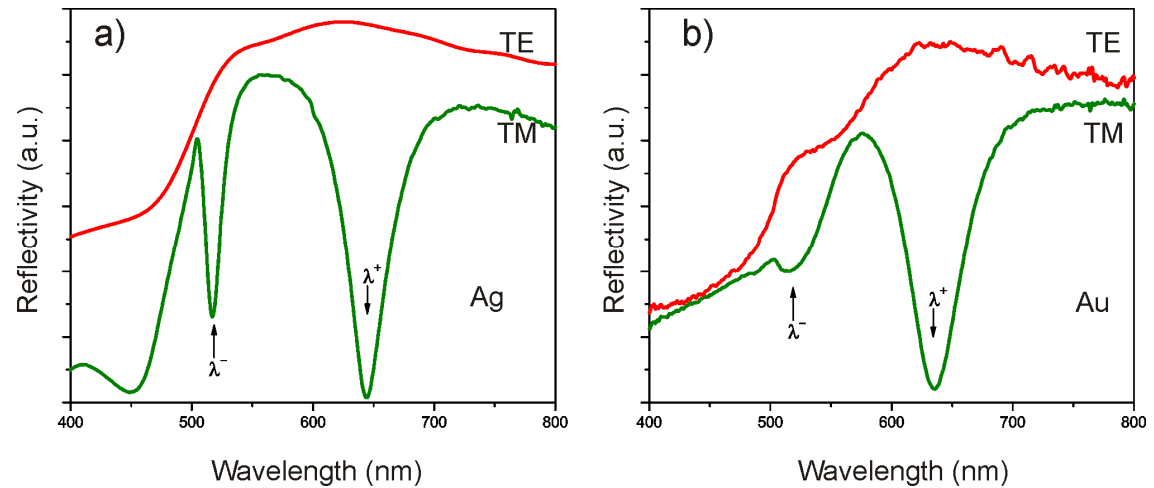
Figure 5.3 Reflectivity spectra for biharmonic gratings coated with metallic film (a) Ag and (b) Au.

5.3. Plasmonic Density of States

Figure 5.4 shows the dispersion diagrams of biharmonic and uniform grating structure. It is clearly seen that biharmonic grating has a band gap, where as the uniform one has crossing bands. Plasmonic density of states as

$$D(\omega) = \sum_{Bands} \sum_{k_{SPP}} \delta(\omega - \operatorname{Re} \omega(k_{SPP})) \sim \frac{dk}{d\omega} \qquad 5.1$$

Where k is the wave vector and ω is the frequency of the surface plasmon. Density of states depends on the flatness of the bands and band gap formation flattens the dispersion curve. Dispersion of biharmonic gratings have flat band around upper band edges.
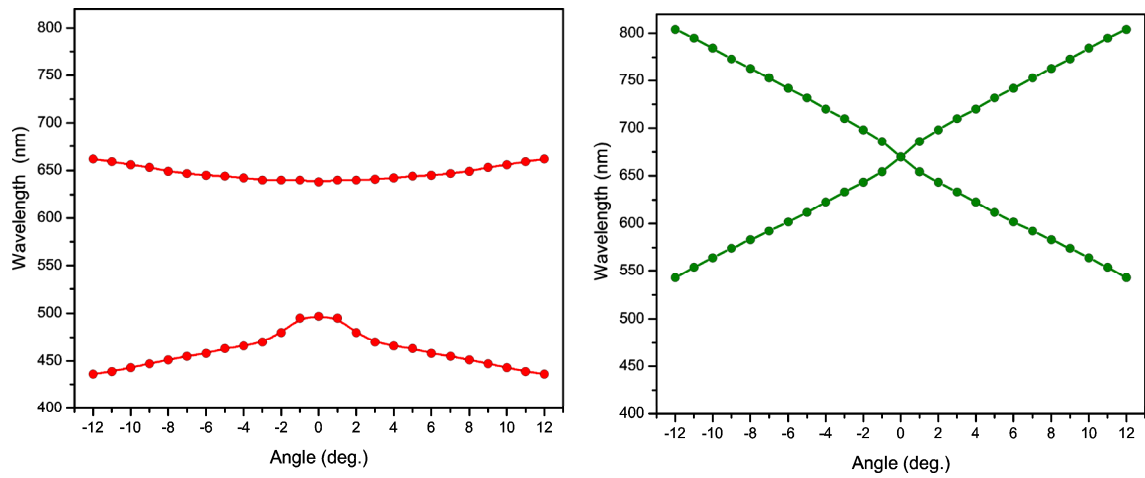
Figure 5.4 Experimental dispersion diagrams for (a) biharmonic and (b) uniform grating structures.

Increased density of state changes the bandwidth of the coupling angle of the emitted Raman signal on the grating surface. Figure 5.5 schematically represents this coupling event. Efficiently excited SPP's then scattered in the vertical direction. The collection optics (microscope objective) allows collecting these re radiated Raman signal. This is the reason behind the enchantment of Raman signal.
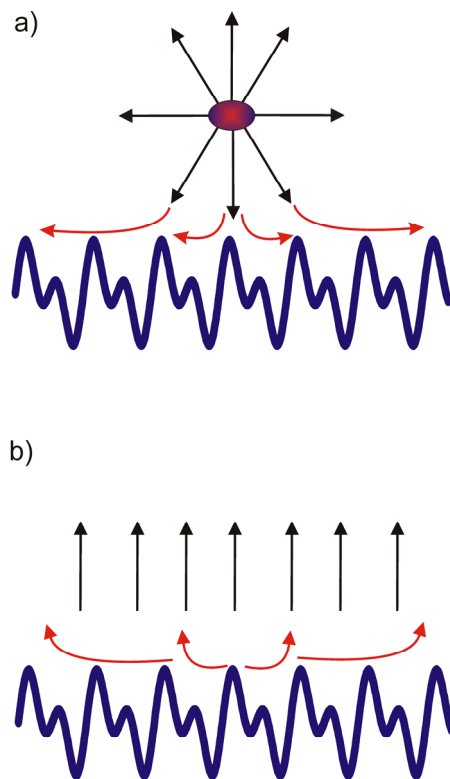
Figure 5.5 A schematic representation of SERS enhancement mechanism on biharmonic grating. (a) Emitted Raman signals efficiently couple to the SPP and then (b) SPP re-radiated in vertical direction.

5.4. Surface Enhanced Raman Scattering

Raman spectra were obtained with a Jobin Yvon LABRAM Raman Spectrometer equipped with a He-Ne laser with an excitation line at 632.81 nm. The incident power was 20 mW and the laser beam was focused by a 10x objective lens. The scattered radiation was collected by the same objective lens and sent via a Raman notch filter to a Peltier cooled CCD detector. 10 μl of 10^{-6} M Rodamine 6G (see the inset of Fig. 5.6) solutions were drop-coated onto the template and were then allowed to dry. A typical spectrum taken from the biharmonic metallic grating is shown in Fig. 5.6. The SPP absorption spectrum at normal incidence and the SERS spectrum of R6G molecule are shown as green and red curves in Fig. 5.6, respectively. Raman bands at 616, 777, 1191 cm^{-1} associate with C-C-C ring in-plane, out of plane bending and C-C stretching vibrations, respectively, as well as bands at 1364, 1512 and 1653 cm^{-1} which are usually assigned to aromatic C-C stretching vibrations of R6G molecule [85]. After the molecular deposition, effective index of the SPP environment slightly changes. This makes plasmonic absorption shift towards the longer wavelengths by about 10 nm. After subtracting the background, empirical signal enhancement factors were determined using peak integrated ratios of the surface enhanced Raman vibration to the corresponding unenhanced signal from 55 nm-thick Au metal surface coated on Si surface. Enhancement factor of 10^5 which is 10 times better than that of uniform grating surfaces was measured.
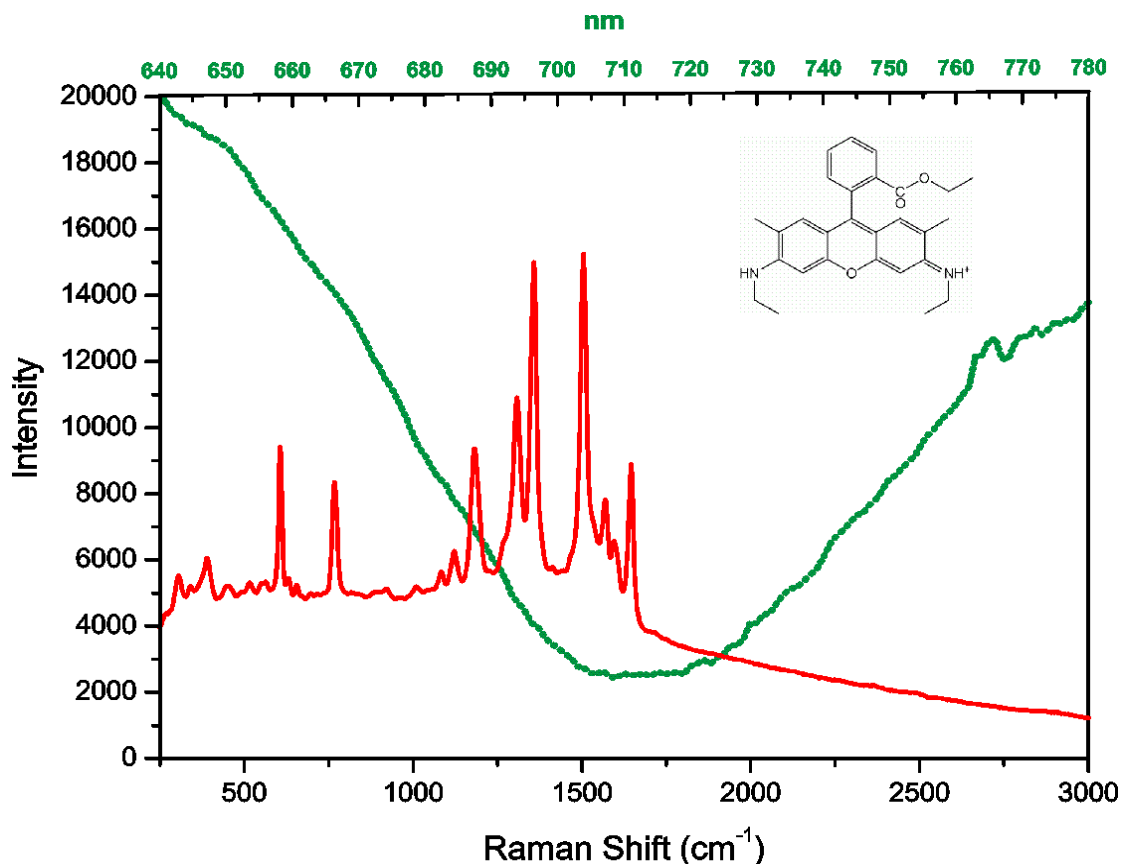
Figure 5.6 SERS spectrum of 10^{-6} M R6G spectrum taken from the biharmonic surface coated with Au metal with an integration time of 1s (Red curve). Green curve represents the normal incidence reflectivity of biharmonic plasmonic template. Inset shows the molecular structure of R6G molecule.

Resonance absorption wavelength dependence of SERS signal can provide a key insight into the mechanism leading to SERS enhancement. We observed that grating strength can strongly perturb the plasmonic band gap properties. We chose this approach to tune the resonance wavelength rather than changing the periodicities of the grating components. Different templates having various exposure times during interference lithography stage, hence with different strengths, were prepared. The reflection spectra of these templates are shown in Fig. 5.7.a. We observed a shift of the reflection resonance as a function of the grating strength by about 100 nm allowing the tuning of plasmonic resonance through the Stokes shifted Raman lines of the compound under study. SERS measurements were performed by following the same procedure described before and SERS spectra were shown in Fig. 5.7.b. When the resonance wavelength is close to the Stokes signal, higher enhancement values were calculated. Minimum enhancement occurs when the resonance absorption is close to the laser line. At a first glance, this response looks different than previously reported behavior for the case of nano-particles [20]. When metallic nanoparticles are used as SERS substrate, maximum SERS enhancement is obtained when plasmonic resonance absorption lies between laser line and Raman emission wavelengths. However, in our case, enhancement is caused by the localized field and is not as high as it occurs at the near field of the metallic nanoparticles. On biharmonic plasmonic templates, plasmon coupled enhancement mechanism is a strong factor than the field enhancement factor as observed in this study.
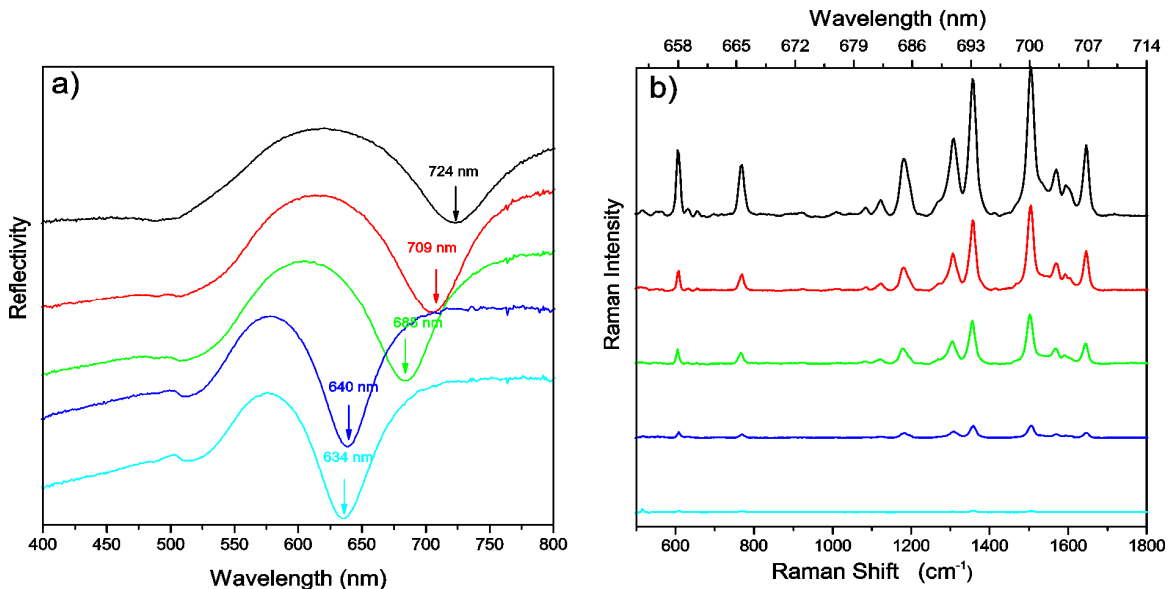
Figure 5.7 (a) Resonance absorption spectra of biharmonic metallic gratings with different grating strength. (b) Corresponding SERS spectra for each resonance conditions (Background subtracted and spectra are all shifted for a better view).

5.5. Enhancement of Photoluminescence

In addition to the SPP coupled emission enhancement on the biharmonic grating study, photoluminescence measurements were performed. Prepared biharmonic metallic surfaces were deposited with a 20 nm thick silicon rich silicon nitride film. Due to the formation of silicon clusters, as deposited silicon nitride has a broad emission spectrum ranging from 500 nm to 800 nm. Experiments were performed at room temperature using Ar^+ laser operating at 488 nm wavelength. Samples were illuminated with the laser and emission was collected in the backscattering configuration and analyzed using a 1-m double spectrometer equipped with photon counting electronics. The emission spectrum of silicon rich silicon nitride film on a flat silicon substrate and the photoluminescence spectrum obtained on the

biharmonic surface are shown in Fig. 5.8 as brown and green curves, respectively. The reflection spectrum of the biharmonic surface (red curve) is also superimposed on Fig. 5.8 to display the contrast with the photoluminescence enhancement. Figure 6 clearly shows the correlation between plasmonic absorption and enhancement in directional emission of photoluminescence. Photoluminescence spectrum mimics the features of the reflection spectrum both in wavelength and the width of the peaks. The enhancement mechanism is based on the excitation of SPPs on the metal surface [86-88]. Emitted photon couples to the SPPs through higher grating components (Λ_1=500 nm) or near field effects. We note that, due to the second harmonic component (Λ_1=250 nm) a plasmonic band gap is formed and SPP density of states (DOS) are increased in the vicinity of the band edges. Flat dispersion profile around band edges increases the DOS and leads to effective energy transfer [89, 90]. Excited SPPs then scatter into photon states through the grating. It can be calculated from Fig. 5.8 that biharmonic grating can have directional enhancement by a factor of 30.
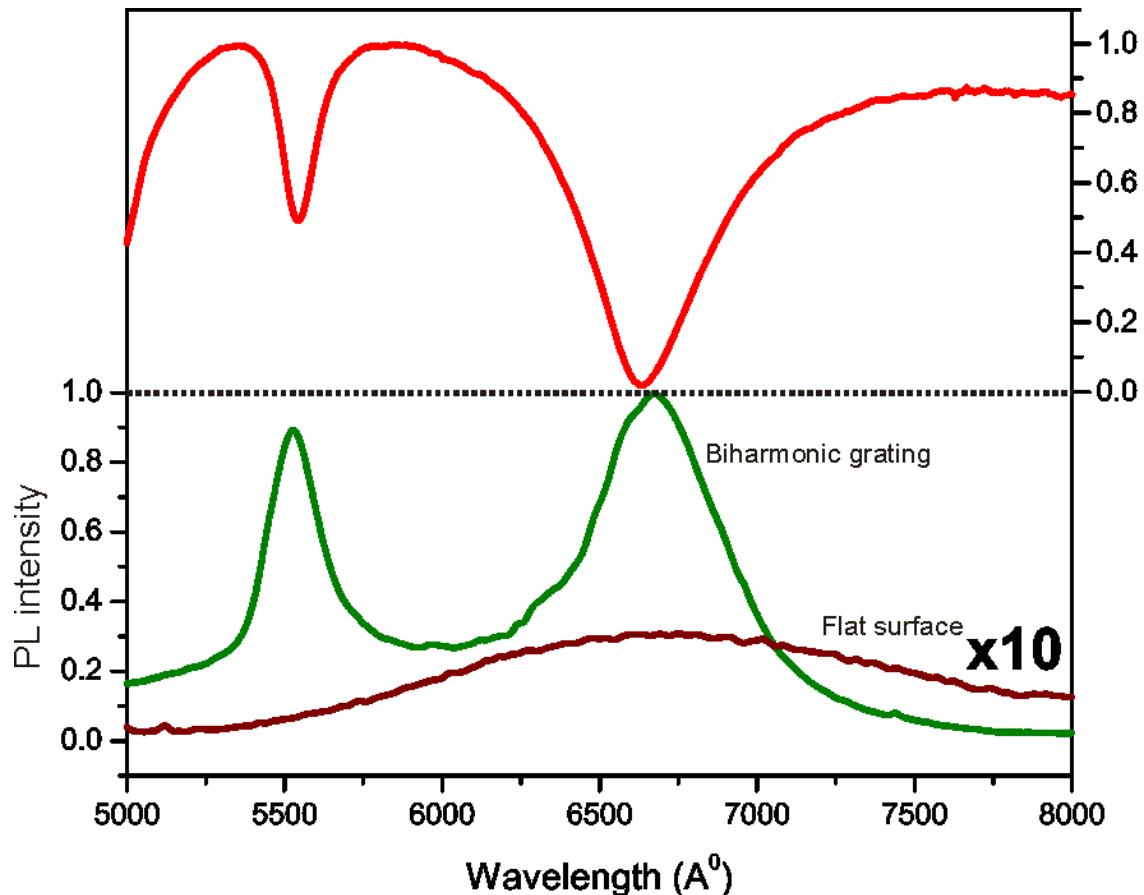
Figure 5.8 Normal incidence PL spectrum of biharmonic metallic grating coated with silicon rich silicon nitride. Red curve represents the plasmonic absorption and green curve shows the PL spectrum. There is 30 times enhancement in PL signal at wavelengths coinciding with the plasmonic resonance wavelengths. Brown curve indicates 10 times magnified broad band emission spectrum of silicon rich silicon nitride film on the flat Si surface.

5.6. Conclusion

We have shown that biharmonic gratings can be used as templates for SERS and photoluminescence enhancement. Due to the plasmonic band gap formation, biharmonic grating surfaces, improve the SPP excitation at the vicinity of the band edges and reveal SERS enhancement factors up to 10^5. The gratings are stable in air and water at ambient temperatures and show no appreciable loss in SERS activity over a period of several months. The adsorption of analytes is reversible, such that the substrates can be used many times. In addition, the SERS enhancements are reproducible between replicate samples with relative standard deviations of approximately 10%. Such features complement the tunable SERS properties of biharmonic gratings and enhance their potential value for routine chemical and biological sensing. Finally, we showed that grating strengths can be used to tune the plasmonic resonance to optimize the enhancement in Raman signal. We have demonstrated that SPP coupled enhancement is the dominant physical mechanism in our templates.

Chapter 6

Plasmonic Band Gap Cavities on Moiré Surfaces

In this chapter, we report on demonstration coupled plasmonic cavities on metallic Moiré surfaces. Moiré surfaces consist of two superimposed gratings with closely spaced periodicities and are represented with sinusoidally modulated amplitude that includes a phase shift of π located at the node. Acting as a cavity, this phase shift localizes the propagating surface plasmons about the node. Furthermore, sinusoidally modified amplitude around the cavity region suppresses the radiation losses and reveals a relatively high quality factor (Q=103). When the cavities are placed close to each other, coupling between plasmonic cavities takes place and a unique low dispersive wave guiding mode resulting in a slowly propagating SPP in the band gap region is observed. Dispersion characteristics of this mode can be described by the tight binding model. Finally, we have shown that on metallic Moiré surfaces, propagating surface plasmons have group velocities

around $v_g \sim 0.44c$ at the center of the wave guiding band and approach to zero at the band edges.

6.1. Phase Shifted Grating Surfaces

Electrical field intensity in optical materials is inversely proportional to the group velocity (v_g) of the propagating light at constant power [91-93]. Hence, small group velocities can enhance nonlinear processes [94-98] and improve optical conversion efficiencies [99]. Among several approaches, the use of photonic crystals has been the main route to manipulate group velocity. One and two dimensional periodic refractive index modulation can form a photonic crystal which allows specific optical modes and suppresses others in the same medium. Regions of mode suppression are known as photonic band gaps. The characteristics of all modes are defined by dispersion diagrams. Close to the vicinity of the photonic band edges dispersion diagrams flatten and reveal a reduction in group velocity [96]. Furthermore, line defect photonic crystal also strongly modifies the group velocity in the vicinity of the cutoff wavelength [96, 97, 100]. Alternatively, photonic crystal nano cavities can be used as a slow light medium [101, 102]. These approaches do not always allow the desired control on dispersion characteristics corresponding to reduced speed for propagating light. Design of unique dispersion profiles may be possible by coupled resonator optical waveguides cavities (CROWs) [91, 103-106]. On the other hand, plasmonic cavities have recently been demonstrated using selective dielectric loading of plasmonic structures [107]. Additionally, Bragg reflectors have been used to observe plasmonic cavity [32] and plasmon hoping along cavities [108]. Previously, propagating surface plasmons with small group velocities have been observed in the vicinity of the band edges of periodic structures [109, 110]. In this work, we demonstrate plasmonic cavities as

well as coupling between the cavities on metallic Moiré surfaces for propagating SPPs with features similar to CROW structures. We show the design, fabrication and the use of these surfaces to obtain propagating SPPs with small group velocities. By adjusting the coupling strength between the cavities, we study both weakly and strongly coupled regimes. We show that tight binding description previously applied to CROW structures is also suitable for the weakly coupled plasmonic cavities.
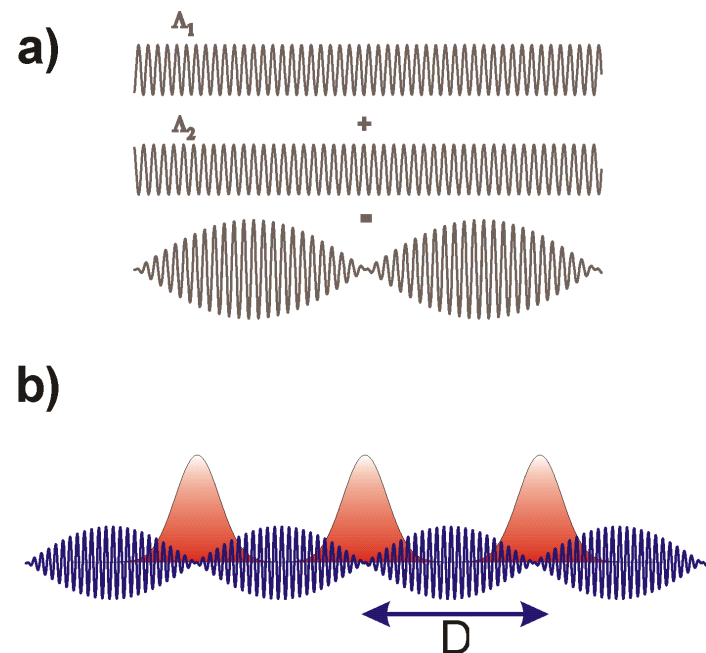
Figure 6.1 Localization of a surface plasmon on a Moiré surface. a, Superimposed two uniform gratings with different periodicities result in a Moiré surface. b, Schematic representation of the Moiré surface as a basis of plasmonic coupled cavities. Red peaks show the localized plasmonic cavity modes.

Figure 6.1.a shows the Moiré pattern formed by two superimposed uniform periodic structures having periodicities close to one another [111]. Superimposed periodicities add up to produce nodes and antinodes at the beat frequency of interfering periods and create an additional super periodicity. As seen in Fig. 6.1.b, the vicinity of the nodes where the amplitude modulation approaches to zero forms a cavity. The final Moiré surface profile can be expressed as

$$S(x) = \cos(Gx)\sin(gx) \qquad (6.1)$$

where $g = \dfrac{2\pi}{d} = 2\pi\dfrac{\Lambda_1 + \Lambda_2}{2\Lambda_1\Lambda_2}$, $G = \dfrac{2\pi}{2D} = 2\pi\dfrac{\Lambda_1 - \Lambda_2}{2\Lambda_1\Lambda_2}$, d, D are the uniform periodicity and the periodicity of the superstructure (half periodicity of the envelope function), respectively. Λ_1 and Λ_2 are the periodicities of the superimposed uniform gratings. The basic physical principle underlying the cavity behavior of Moiré surface is based on the π phase shift experienced by the SPPs while propagating between the nodes [112, 113]. The cosine term in Eq. 6.1 acts as an envelope function and modulates the amplitude of the grating surface. Envelope function changes sign at the node of the grating and creates a spatial π phase shift. We have fabricated the Moiré patterns using a conventional interference lithography system. Successive exposures at different illumination angles result in a Moiré surface on the photosensitive polymeric surface.

Shown in Fig. 6.2a is the AFM image of the fabricated Moiré surface. Surface includes two slightly different periods with periodicities of Λ_1= 295 nm and Λ_2=305 nm that result in a

superimposed grating. Figure 6.2.b indicates the line profile of the AFM image. Red dots represent the uniform periodicity (*sin(gx)*) of 300 nm. It is clearly seen that at the left side of the pattern red dots coincide with the peaks and while on the right side, red dots coincide with the troughs of the pattern. This indicates the presence of π phase shift located at the node. This phase shift makes Moiré surface act as a distributed Bragg reflector (DBR) with sinusoidally modulated amplitude. Figure 6.2.c shows the power spectrum of the line profile clearly indicating the two different harmonic components belonging to the superimposed gratings. These types of structures have been studied in optical waveguides, fiber based devices and filters with narrow and rectangular–shaped reflection/transmission spectra [111-113].
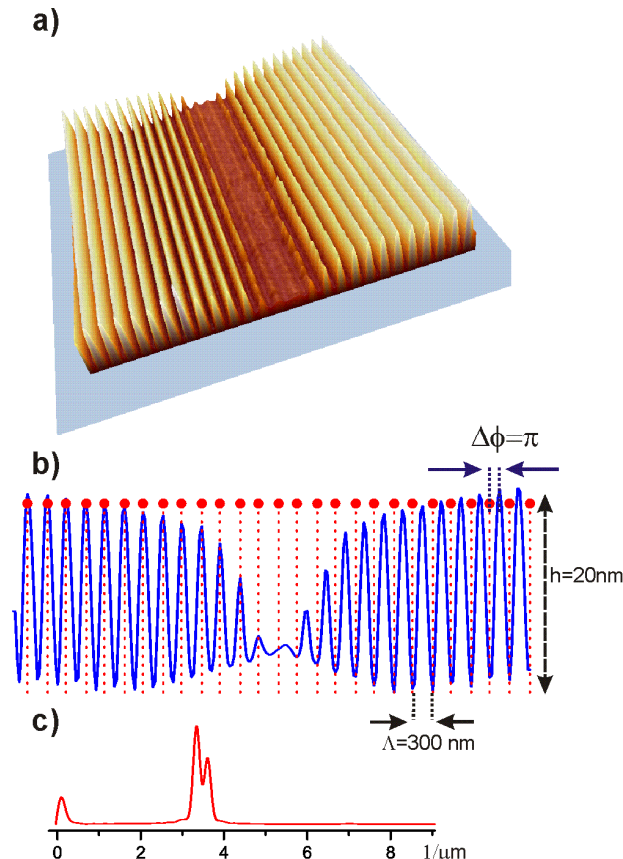
Figure 6.2 Moiré surface. (a) 2D AFM image of a typical Moiré surface. (b) Line profile of AFM image, red dots represents the uniform periodicity and π phase shift occurs at the node of the surface. (c) Power spectrum of the Moiré surface indicating two grating components.
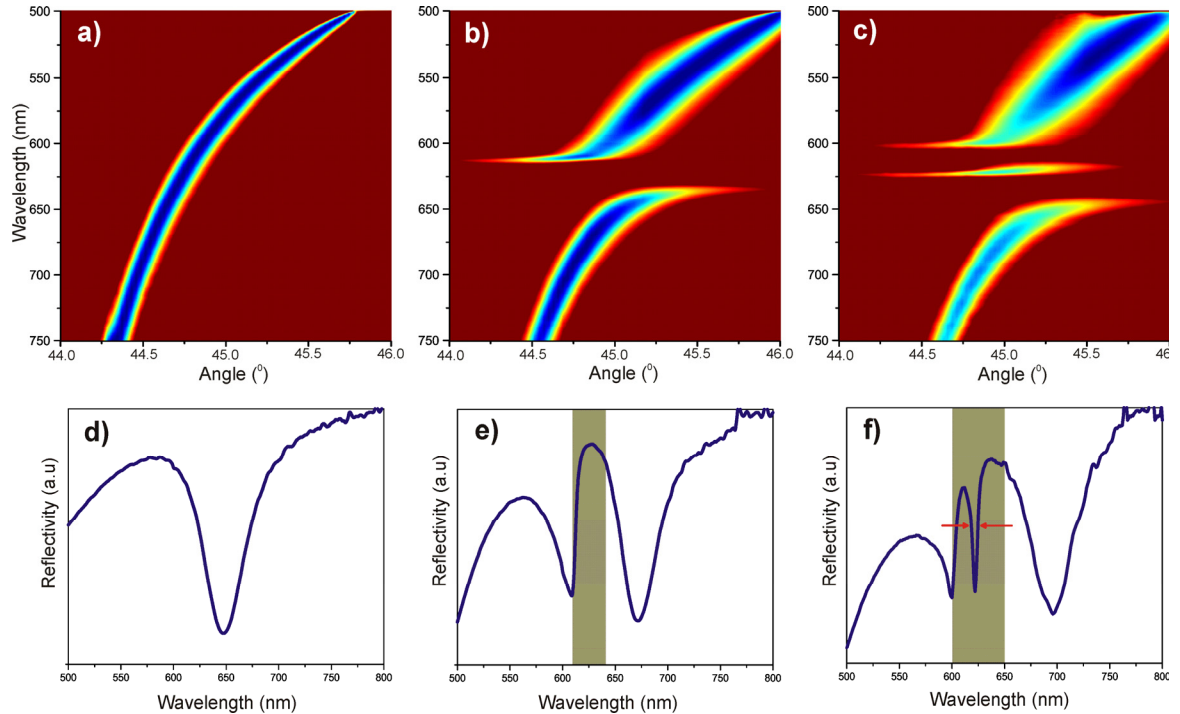
Figure 6.3 Measured dispersion curves of SPP's on periodic structures. Experimental dispersion curves of SPP's on (a) flat metal surface, (b) uniform grating, (c) Moiré surface, (d), (e), (f), shows the reflectivity of the samples at a constant incidence angle of 45^0 for each dispersion curves given in (a), (b), (c) respectively. In (d) and (f) highlighted areas indicate the plasmonic band gap region.

To study the plasmonic localization and CROW type wave guiding on Moiré surfaces, angle and wavelength dependent reflectivity was measured. In order to construct the band structure, the reflectivity was measured as follows; A spectroscopic ellipsometer (WVASE32) was used to measure the reflection in the visible wavelength range. Kretschmann configuration was used to compensate the momentum mismatch between the incoming light and excited plasmon on Au-air interface. Plasmonic surfaces were fabricated on a transparent glass substrate and coated with 50 nm thick Ag film. Sample

was then attached onto the prism using index matching fluids. Sample was illuminated from prism side and wavelength dependent reflectivity measurements were taken with different incidence angles from which two dimensional reflectivity maps were constructed. In plane wave vector of the SPP depends on the incidence angle and can be tuned by changing the incidence angle between surface of the prism and incoming light. Finite set of measurements were interpolated using linear interpolation algorithm with MATLAB.

We note that when surface plasmons at Au-air interface are excited, angle dependent reflectivity reveals the dispersion characteristics of plasmonic modes. On flat metal surfaces, it is possible to excite SPPs at all wavelengths in the visible range at specific incidence angles. Dispersion on a flat surface asymptotically converges to the surface plasmon resonance frequency of $\omega_p/\sqrt{2}$ where ω_p is the bulk plasmon frequency. Figure 6.3.a shows experimental reflectivity map of flat metal surfaces indicating the dispersion diagram. Effective refractive index of the surface plasmon is highly dispersive in the visible wavelength range. At a given angle, this dispersive behavior restricts the excitation of SPP's in a wide wavelength range. Figure 6.3.d shows the wavelength dependent reflectivity at a specific incidence angle. The dip in reflectivity spectrum indicates the SPP excitation. It should be noted that excitation strengths are different for each wavelength due to the dispersion mentioned above.

Periodic metallic structures can scatter the propagating SPPs in the backward direction and form a standing wave. This standing wave formation opens a band gap in the dispersion diagram [2, 41]. In order to observe this, we fabricated a uniform metallic grating structure having a periodicity around 300 nm. Same reflectivity measurements were performed for

periodically modulated samples. Reflectivity map in Fig. 6.3.b shows a summary of the experimental results. As expected, band gap formation is clearly observed in the dispersion diagram. Dispersion of the band flattens at the vicinity of the band edge. SPP's having a wavelength at band edges create a standing wave localized on the grating structure. Energy difference between the band edges originates from different mode localization profiles, the lower energy configuration corresponding to localization at the peaks of the grating while the higher energy configuration corresponds to localization of the mode on the troughs [41]. As seen in Fig. 6.3.e, the reflectivity increases inside the SPP excitation region. This reflectivity increase means SPP excitation in this wavelength range is suppressed due to the band gap. Colored area indicates the band gap region.

6.2. Slowing Down the Surface Plasmon on a Moiré Surface

To extract the full plasmonic band diagram including the characteristics of the localized mode from the Moiré pattern a further experiment was performed. A non-dispersive flat band in the band gap is a key feature of a localized plasmon in a cavity. On the other hand, if individual localized modes start to overlap due to cavity-to-cavity coupling, energies of the corresponding modes split into a new configuration. Furthermore, if these cavities form a periodic structure, linear combination of the individual modes satisfies the Bloch condition and forms a mini dispersive wave guiding band inside the photonic band gap zone. This phenomenon is called coupled resonator optical wave guiding. This is where the similarity between the Moiré pattern and CROW structure starts. As described before, the vicinity of the nodes where there is a phase shift of π, acts as a cavity. If the super periodicity is small enough to create a coupling between cavities, a Moiré surface can be modeled as a CROW.

Figure 6.3.c shows the dispersion diagram extracted from the reflectivity map of the Moiré surface. A slight but clearly noticeable dispersive localized mode appears inside the band gap region. This band indicates the presence of a wave guiding mode of the coupled plasmonic cavities. This energy band can be modeled by using the tight binding approach well known in solid state physics and applied to CROW type devices. The simplified expression of the dispersion obtained from the tight binding approximation can be written as [91]

$$\omega(k) = \Omega\big[1 + \kappa\cos(kD)\big] \tag{6.2}$$

where D, Ω, κ are the super periodicity of the cavities, the resonance frequency of individual cavity and coupling factor, respectively. Upon closer inspection of Fig. 6.3.c, we find that the dispersion of the localized mode can be fit by the dispersion equation obtained from the tight binding approximation. The coupling coefficient between the cavities can be expressed as $\kappa = \Delta\omega/2\Omega$ $\Delta\omega$ is the CROW band width and resulting $\kappa \sim 0.006$. The small value of the coupling coefficient displays the weak nature of the coupling between the cavities.
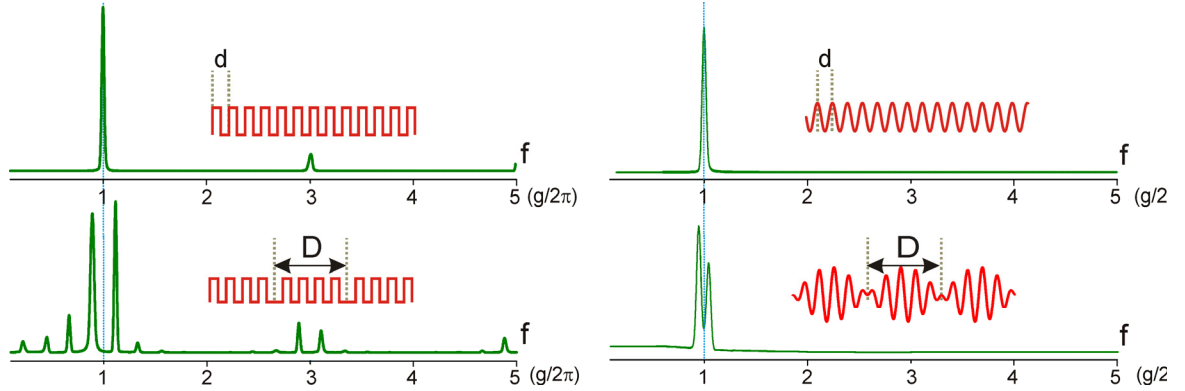
Figure 6.4 Fourier spectrum of different grating structures which shows the similarity between the DBR cavity geometry and the Moiré surface.

We then study the wavelength dependence of the localized mode in the reflectivity spectrum in Fig. 6.3.f and find that the sharp plasmonic excitation has a very small line width of $\Delta\lambda = 6\,\text{nm}$. The 6 nm line width corresponds to a quality factor of Q=103. This quality factor is relatively high for plasmonic cavities [32, 107, 108]. The reason behind this improvement is the suppression of the radiative losses. The overall quality factor can be described as[56]

$$\frac{1}{Q} = \frac{1}{Q_{abs}} + \frac{1}{Q_{rad}}$$

(6.3)

where Q_{abs} and Q_{rad} are the radiative and absorptive quality factors respectively. Q_{abs} is dominated by the metallic loss in the plasmonic cavities and Q_{rad} by out of plane radiative

losses. In general, radiative loss due to leaky modes is caused by scattering of the surface plasmon from higher order grating harmonics and the abrupt change of the localized mode profile in the cavity region [4]. Moiré pattern allows us to get rid of both of these radiative loss sources. As seen in Fig. 6.2.c, it includes only two harmonic components which can not create significant out-of-plane scattering. Additionally, due to the smooth sinusoidal-like amplitude modulation, the higher wave vector components inside the localized cavity mode are suppressed [4].

To analyze the dispersion characteristics of the coupled cavity wave guiding, we tracked the position of the SPP excitation wavelength. The measured dispersion diagram is shown in Fig. 6.5.a (Red dots). It is seen that dispersion band gets flattened at the edges of the mini band. The group velocity can be expressed as $v_g = d\omega/dk$. The green dots in Fig. 6.5.a show the group velocity throughout the band. The group velocity is around $v_g = 0.44c$ at the center of the band and approaches to zero in the vicinity of the band edges.
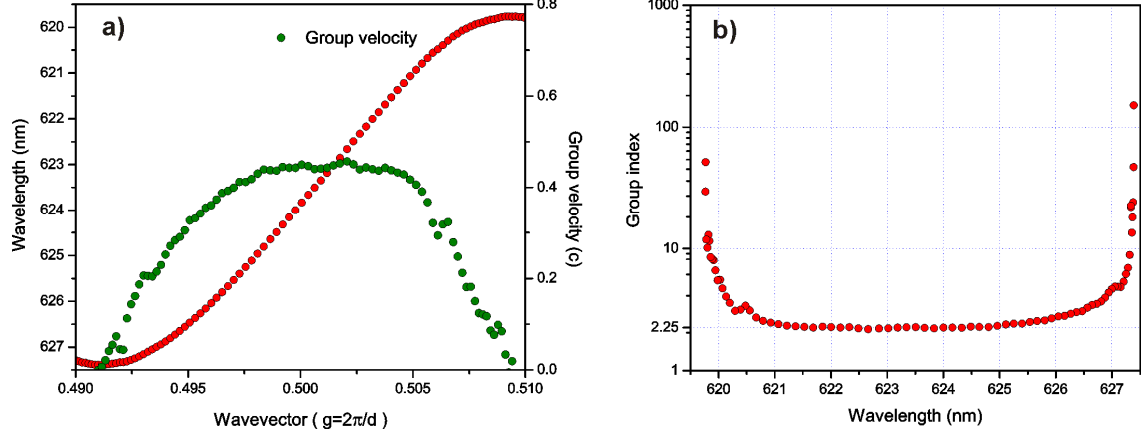
Figure 6.5 Measured dispersion curves, group velocity and group indices of SPP's on Moiré surfaces. (a) red dots show the experimental dispersion curve of wave-guiding mode on a Moiré surface indicating CROW type dispersion and green dots show the corresponding group velocities. (b) Measured group indices as a function of wavelength for CROW type mode.

The behavior of the group velocity can also be understood within the framework of the tight binding approach. Since the dispersion of the band is given by Eqn. 6.2, the group velocity is[5]

$$v_g(k) = -\Omega D\kappa \sin(kD) \tag{6.4}$$

where D, Ω , κ are the super periodicity of the cavities, the resonance frequency of individual cavity and coupling factor, respectively. As seen in Fig. 6.5.a, group velocity shows a sinusoidal profile as expected from the tight binding approximation. The significant factor in the magnitude of group velocity is the coupling coefficient (κ). It is clear that small values (κ) result in very low group velocities. Figure 6.5.b indicates the corresponding group index ($n_g = c/v_g$) of the SPPs which is nearly constant in the center of the wave guiding band and increases dramatically at the band edges.
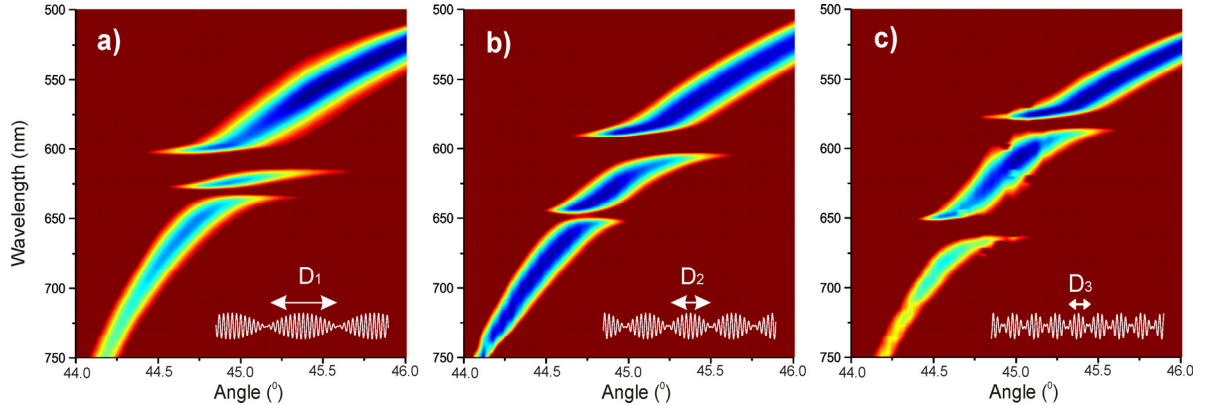
Figure 6.6 Measured dispersion curves of SPP's on Moiré surfaces having different super periodicities. (a), (b), (c) shows dispersion curves for different D values of 7.5, 4.5, 2.5 μm, respectively. Increased coupling between the cavities leads to the appearance of a normal dispersion band in the band gap.

Finally, we have also investigated the strong coupling regime of the Moiré cavities. In the strong coupling regime, the mini band should converge towards normal plasmonic dispersion around the center of the band. In a Moiré pattern, strength of the cavity coupling can be controlled by changing the distance between plasmonic cavities. Cavity-to-cavity distance $D = (\Lambda_1 \Lambda_2)/(\Lambda_1 - \Lambda_2)$ depends on the difference between the periodicities of superimposed gratings.

Shown in Fig. 6.6 are the band diagrams, corresponding to three different Moiré surfaces with three different beat frequencies, resulting in increased coupling between the cavities. In Fig. 6.6.a, periodicities of the gratings are close to each other than that shown in Fig. 6.6.c. As the distance between the nodes of the Moiré pattern decreases, the coupling coefficient increases and the center of the wave guiding band approaches towards normal plasmonic dispersion. However, bending of the dispersion curve at the band edges is also

observed. In this strong coupling regime, Moiré pattern behaves more like two independent gratings creating two different band gaps. With proper choice of the envelope function, one can engineer the characteristics of the dispersion in the band gap of the coupled cavity system.

In conclusion, we have shown that metallic Moiré surfaces act as a cavity and localize the propagating surface plasmon due to the π phase shift at its nodes. Sinusoidally modified amplitude around the cavity region suppresses the radiation losses and reveals a relatively high factor (Q=103). Furthermore, weakly coupled cavities form a low-dispersion wave guiding mode and results in slowly propagating SPP in the band gap region. We have demonstrated that dispersion characteristics of this mode can be described by the tight binding model and dispersion properties strongly depend on the coupling strength of the cavities. The cavity to cavity distance allows tuning of the coupling strength and enables us to engineer the dispersion characteristics of the SPP. Small group velocities and confined behavior of SPP are promising for plasmonic nonlinear applications.

Chapter 7

Conclusions

In conclusion, in this thesis we have demonstrated two different approaches to fabricate plasmonic band gap cavities. First approach is based on biharmonic gratings. Biharmonic gratings consist of two different gratings. First grating component is used to couple light to surface plasmons and the second grating is superimposed onto the first to create a band gap at the excitation wavelength of the first grating. Cavity formation requires controlling the optical properties of SPP. High dielectric superstructures is used to perturb the effective index of the propagating SPP. We showed that the band gap widths of grating based plasmonic structures can be controlled with the deposition of high dielectric layers. By selective deposition, we have demonstrated the formation of plasmonic cavities. We observe cavity modes both in the infrared and the visible part of the spectrum. The approach we use is simple, combining holographic lithography with photolithography to fabricate plasmonic band gap cavities. This approach is suitable for large area applications and makes plasmonic cavities applicable in many fields of study.

Additionally, we have also shown that biharmonic gratings can be used as templates for SERS and photoluminescence enhancement. Due to the plasmonic band gap formation, biharmonic grating surfaces, improve the SPP excitation at the vicinity of the band edges and reveal SERS enhancement factors up to 10^5. The gratings are stable in air and water at

ambient temperatures and show no appreciable loss in SERS activity over a
period of several months. The adsorption of analytes is reversible, such that the substrates
can be used many times. In addition, the SERS enhancements are reproducible between
replicate samples with relative standard deviations of approximately 10%. Such features
complement the tunable SERS properties of biharmonic gratings and enhance their
potential value for routine chemical and biological sensing. Finally, we showed that grating
strengths can be used to tune the plasmonic resonance to optimize the enhancement in
Raman signal. We have demonstrated that SPP coupled enhancement is the dominant
physical mechanism in our templates.

Alternatively, we show that metallic Moiré surfaces can also serve as a basis for plasmonic
cavities with relatively high quality factors. We have demonstrated localization and slow
propagation of surface plasmons on metallic Moiré surfaces. Phase shift at the node of the
Moiré surface localizes the propagating surface plasmons in a cavity and adjacent nodes
form weakly coupled plasmonic cavities. We demonstrate that group velocities around v =
0.44c at the center of the coupled cavity band and almost zero group velocity at the band
edges can be achieved. Furthermore, sinusoidally modified amplitude about the node
suppresses the radiation losses and reveals a relatively high quality factor of Q=103 for
plasmonic cavities. We have shown that dispersion strongly depends on the coupling
between the cavities.

Finally, the research initiated in this thesis in the field of grating based cavities opens up a
whole new area of possibilities. Some of these such as the study of the effects of grating
strength on plasmon resonance, electrical and mechanical tuning of plasmon resonance and
their applications to SERS, two dimensional biharmonic gratings and their cavities are in
progress are expected to bear fruit very soon. Finally, interaction of surface plasmons with

nonlinear dielectric surfaces and dynamics of plasmonic cavities are being studied by my group members.

Bibliography

1.   H. A. Atwater, "The promise of plasmonics," Sci. Am. **296**, 56-63 (2007).

2.   W. L. Barnes, A. Dereux, and T. W. Ebbesen, "Surface plasmon subwavelength optics," Nature **424**, 824-830 (2003).

3.   W. A. Murray, and W. L. Barnes, "Plasmonic materials," Adv. Mater. **19**, 3771-3782 (2007).

4.   Y. Akahane, T. Asano, B. S. Song, and S. Noda, "High-Q photonic nanocavity in a two-dimensional photonic crystal," Nature **425**, 944-947 (2003).

5.   H. Altug, D. Englund, and J. Vuckovic, "Ultrafast photonic crystal nanocavity laser," Nat. Phys. **2**, 484-488 (2006).

6.   D. Englund, A. Faraon, I. Fushman, N. Stoltz, P. Petroff, and J. Vuckovic, "Controlling cavity reflectivity with a single quantum dot," Nature **450**, 857-861 (2007).

7.   E. Chow, A. Grot, L. W. Mirkarimi, M. Sigalas, and G. Girolami, "Ultracompact biochemical sensor built with two-dimensional photonic crystal microcavity," Opt. Lett. **29**, 1093-1095 (2004).

8.   K. Lee, and S. A. Asher, "Photonic crystal chemical sensors: pH and ionic strength," J. Am. Chem. Soc. **122**, 9534-9537 (2000).

9.   H. Atwater, "Subwavelength scale photonic devices.," Abstr. Pap. Am. Chem. S. **227**, U480-U480 (2004).

10. J. A. Dionne, L. A. Sweatlock, H. A. Atwater, and A. Polman, "Planar metal plasmon waveguides: frequency-dependent dispersion, propagation, localization, and loss beyond the free electron model," Phys. Rev. B **72**, 075405 (2005).

BIBLIOGRAPHY

11.   N. Fang, H. Lee, C. Sun, and X. Zhang, "Sub-diffraction-limited optical imaging with a silver superlens," Science **308**, 534-537 (2005).   85

12.   S. A. Maier, M. L. Brongersma, P. G. Kik, S. Meltzer, A. A. G. Requicha, and H. A. Atwater, "Plasmonics - A route to nanoscale optical devices," Adv. Mater. **13**, 1501 (2001).

13.   D. O. S. Melville, and R. J. Blaikie, "Super-resolution imaging through a planar silver layer," Opt. Express **13**, 2127-2134 (2005).

14.   R. H. Ritchie, "Plasma Losses by Fast Electrons in Thin Films," Phys. Rev., 874 (1957).

15.   R. W. Wood, "On a remarkable case of uneven distribution of light in a diffraction grating spectrum," Phil. Mag., 396 (1902).

16.   M. E. Stewart, C. R. Anderton, L. B. Thompson, J. Maria, S. K. Gray, J. A. Rogers, and R. G. Nuzzo, "Nanostructured plasmonic sensors," Chem. Rev. **108**, 494-521 (2008).

17.   W. R. Holland, and D. G. Hall, "Frequency-Shifts of an Electric-Dipole Resonance near a Conducting Surface," Phys Rev Lett **52**, 1041-1044 (1984).

18.   M. Moskovits, J. Chem. Phys. **69**, 4159 (1978).

19.   E. Hutter, and J. H. Fendler, "Exploitation of localized surface plasmon resonance," Adv. Mater. **16**, 1685-1706 (2004).

20.   A. D. McFarland, M. A. Young, J. A. Dieringer, and R. P. Van Duyne, "Wavelength-scanned surface-enhanced Raman excitation spectroscopy," J. Phys. Chem. B **109**, 11279-11285 (2005).

21.   C. Loo, A. Lin, L. Hirsch, M. H. Lee, J. Barton, N. Halas, J. West, and R. Drezek, "Nanoshell-enabled photonics-based imaging and therapy of cancer," Technol. Cancer. Res. T. **3**, 33-40 (2004).

22.   J. Vuckovic, M.Loncar, and A. Scherer, "Surface plasmon enhanced light-emitting diode," IEEE. J.QUANTUM ELECTRON. **36**, 1131 (2000).

BIBLIOGRAPHY

23.   T. W. Ebbesen, H. J. Lezec, H. F. Ghaemi, T. Thio, and P. A. Wolff, "Extraordinary optical transmission through sub-wavelength hole arrays," Nature **391**, 667-669 (1998).

24.   G. Gay, O. Alloschery, B. V. De Lesegno, C. O'Dwyer, J. Weiner, and H. J. Lezec, "The optical response of nanostructured surfaces and the composite diffracted evanescent wave model," Nat. Phys. **2**, 262-267 (2006).

25.   M. L. Brongersma, J. W. Hartman, and H. A. Atwater, "Electromagnetic energy transfer and switching in nanoparticle chain arrays below the diffraction limit," Phys. Rev. B **62**, 16356-16359 (2000).

26.   S. A. Maier, P. G. Kik, H. A. Atwater, S. Meltzer, E. Harel, B. E. Koel, and A. A. G. Requicha, "Local detection of electromagnetic energy transport below the diffraction limit in metal nanoparticle plasmon waveguides," Nat. Mater. **2**, 229-232 (2003).

27.   H. T. Miyazaki, and Y. Kurokawa, "Squeezing visible light waves into a 3-nm-thick and 55-nm-long plasmon cavity," Phys. Rev. Lett. **96**, 097401 (2006).

28.   A. Boltasseva, T. Nikolajsen, K. Leosson, K. Kjaer, M. S. Larsen, and S. I. Bozhevolnyi, "Integrated optical components utilizing long-range surface plasmon polaritons," J. Lightwave Technol. **23**, 413-422 (2005).

29.   A. E. Craig, G. A. Olson, and D. Sarid, "Experimental-Observation of the Long-Range Surface-Plasmon Polariton," Opt. Lett. **8**, 380-382 (1983).

30.   S. A. Maier, and H. A. Atwater, "Plasmonics: Localization and guiding of electromagnetic energy in metal/dielectric structures," J. Appl. Phys. **98**, 011101 (2005).

31.   S. C. Kitson, W. L. Barnes, and J. R. Sambles, "Full photonic band gap for surface modes in the visible," Phys Rev Lett **77**, 2670-2673 (1996).

BIBLIOGRAPHY

32. J. C. Weeber, A. Bouhelier, G. C. des Francs, L. Markey, and A. Dereux, "Submicrometer in-plane integrated surface plasmon cavities," Nano Lett. **7**, 1352-1359 (2007).

33. F. Wooten, *Optical Properties of Solid* (Academic Press, 1972).

34. A. P. Hibbins, B. R. Evans, and J. R. Sambles, "Experimental verification of designer surface plasmons," Science **308**, 670-672 (2005).

35. J. B. Pendry, L. Martin-Moreno, and F. J. Garcia-Vidal, "Mimicking surface plasmons with structured surfaces," Science **305**, 847-848 (2004).

36. H. Raether, *Surface Plasmons* (Springer-Verlag Berlin, 1986).

37. A. R. Zakharian, J. V. Moloney, and M. Mansuripur, "Surface plasmon polaritons on metallic surfaces," Opt. Express **15**, 183-197 (2007).

38. W. L. Barnes, "Surface plasmon-polariton length scales: a route to sub-wavelength optics," J. Opt. A-Pure Appl. Op. **8**, S87-S93 (2006).

39. I. Avrutsky, "Surface plasmons at nanoscale relief gratings between a metal and a dielectric medium with optical gain," Phys. Rev. B **70**, 155416 (2004).

40. J. D. Joannopoulos, R. D. Meade, and J. N. Winn, *Photonic Crystals* (Princeton University Press, New Jersey, 1995).

41. W. L. Barnes, T. W. Preist, S. C. Kitson, and J. R. Sambles, "Physical origin of photonic energy gaps in the propagation of surface plasmons on gratings," Phys. Rev. B **54**, 6227-6244 (1996).

42. J. Homola, S. S. Yee, and G. Gauglitz, "Surface plasmon resonance sensors: review," Sensors and Actuators B-Chemical **54**, 3-15 (1999).

43. J. S. Biteen, L. A. Sweatlock, H. Mertens, N. S. Lewis, A. Polman, and H. A. Atwater, "Plasmon-enhanced photoluminescence of silicon quantum dots: Simulation and experiment," J. Phys. Chem. C **111**, 13372-13377 (2007).

44.   M. Derouard, J. Hazart, G. Lerondel, R. Bachelot, P. M. Adam, and P. Royer, "Polarization-sensitive printing of surface plasmon interferences," Opt. Express **15**, 4238-4246 (2007).

45.   S. I. Bozhevolnyi, and V. S. Volkov, "Observation of propagation of surface plasmon polaritons along line defects in a periodically corrugated metal surface," Opt. Lett. **26**, 734-736 (2001).

46.   H. J. Lezec, J. A. Dionne, and H. A. Atwater, "Negative refraction at visible frequencies," Science **316**, 430-432 (2007).

47.   T. A. Kelf, Y. Sugawara, R. M. Cole, J. J. Baumberg, M. E. Abdelsalam, S. Cintra, S. Mahajan, A. E. Russell, and P. N. Bartlett, "Localized and delocalized plasmons in metallic nanovoids," Phys. Rev. B **74**, 245415 (2006).

48.   U. Kreibig, and M. Vollmer, *Optical properties metal clusters* (Springer, Berlin, 1995).

49.   N. M. B. Perney, F. J. G. de Abajo, J. J. Baumberg, A. Tang, M. C. Netti, M. D. B. Charlton, and M. E. Zoorob, "Tuning localized plasmon cavities for optimized surface-enhanced Raman scattering," Phys. Rev. B **76**, 035426 (2007).

50.   A. V. Zayats, and I. I. Smolyaninov, "Near-field photonics: surface plasmon polaritons and localized surface plasmons," J. Opt. A-Pure Appl. Op. **5**, S16-S50 (2003).

51.   M. Moskovits, "Surface-Enhanced Spectroscopy," Rev. Mod. Phys. **57**, 783-826 (1985).

52.   K. Kneipp, Y. Wang, H. Kneipp, L. T. Perelman, I. Itzkan, R. Dasari, and M. S. Feld, "Single molecule detection using surface-enhanced Raman scattering (SERS)," Phys. Rev. Lett. **78**, 1667-1670 (1997).

53.   S. M. Nie, and S. R. Emery, "Probing single molecules and single nanoparticles by surface-enhanced Raman scattering," Science **275**, 1102-1106 (1997).

BIBLIOGRAPHY

54. J. A. Sanchez, "Distributed feedback grating for surface-plasmon polaritons based on metal nano-groove/ridge arrays," Opt. Lett. **32**, 2330 (2007).

55. B. Wang, and G. P. Wang, "Plasmon Bragg reflectors and nanocavities on flat metallic surfaces," Appl. Phys. Lett. **87**, 013107 (2005).

56. Y. Y. Gong, and J. Vuckovic, "Design of plasmon cavities for solid-state cavity quantum electrodynamics applications," Appl. Phys. Lett. **90**, 033113 (2007).

57. J. A. S. Gil, "Distributed feedback gratings for surface-plasmon polaritons based on metal nano-groove/reidge arrays," Opt. Express **32**, 2330-2332 (2007).

58. Z. W. Liu, Q. H. Wei, and X. Zhang, "Surface Plasmon Interference Nanolithography," Nano Lett. **5**, 957-961 (2005).

59. R. H. Ritchi, E. T. Arakawa, J. J. Cowan, and R. N. Hamm, "Surface-plasmon resonance effect in grating diffraction," Phys. Rev. Lett. **21**, 1530-1533 (1968).

60. S. C. Kitson, W. L. Barnes, and J. R. Sambles, "Full photonic band gap for surface modes in the visible," Phys. Rev. Lett. **77**, 2670-2673 (1996).

61. A. C. R. Pipino, R. P. VanDuyne, and G. C. Schatz, "Surface-enhanced second-harmonic diffraction: Experimental investigation of selective enhancement," Phys. Rev. B **53**, 4162-4169 (1996).

62. A. Kocabas, and A. Aydinli, "Polymeric waveguide Bragg grating filter using soft lithography," Opt. Express **14**, 10228-10232 (2006).

63. R. C. Alferness, C. H. Joyner, M. D. Divino, M. J. R. Martyak, and L. L. Buhl, "Narrowband grating resonator filter inInGaAsP/InP waveguides," Appl. Phys. Lett. **49**, 125-127 (1986).

64. G. C. Schatz, M. A. Young, and R. P. Van Duyne, "Electromagnetic mechanism of SERS," in *Surface-Enhanced Raman Scattering: Physics and Applications*(2006), pp. 19-45.

BIBLIOGRAPHY

65.   E. J. Bjerneld, F. Svedberg, P. Johansson, and M. Kall, "Direct observation of heterogeneous photochemistry on aggregated Ag   90 nanocrystals using Raman spectroscopy: The case of photoinduced degradation of aromatic amino acids," J. Phys. Chem. A **108**, 4187-4193 (2004).

66.   K. A. Bosnick, J. Jiang, and L. E. Brus, "Fluctuations and local symmetry in single-molecule rhodamine 6G Raman scattering on silver nanocrystal aggregates," J. Phys. Chem. B **106**, 8096-8099 (2002).

67.   A. Campion, and P. Kambhampati, "Surface-enhanced Raman scattering," Chem. Soc. Rev **27**, 241-250 (1998).

68.   W. E. Doering, and S. M. Nie, "Single-molecule and single-nanoparticle SERS: Examining the roles of surface active sites and chemical enhancement," J. Phys. Chem. B **106**, 311-317 (2002).

69.   M. Kall, H. X. Xu, and P. Johansson, "Field enhancement and molecular response in surface-enhanced Raman scattering and fluorescence spectroscopy," J. Raman Spectrosc. **36**, 510-514 (2005).

70.   A. M. Michaels, M. Nirmal, and L. E. Brus, "Surface enhanced Raman spectroscopy of individual rhodamine 6G molecules on large Ag nanocrystals," J. Am. Chem. Soc. **121**, 9932-9939 (1999).

71.   M. Kerker, "Electromagnetic model for surface-enhanced Raman scattering (SERS) on metal colloids," Acc. Chem. Res. **17**, 271-277 (1984).

72.   M. Kerker, O. Siiman, L. A. Bumm, and D. S. Wang, "Surface enhanced Raman scattering (SERS) of citrate ion adsorbed on colloidal silver," Appl. Opt. **19**, 3253 (1980).

73.   F. J. GarciaVidal, and J. B. Pendry, "Collective theory for surface enhanced Raman scattering," Phys. Rev. Lett. **77**, 1163-1166 (1996).

BIBLIOGRAPHY

74. H. H. Wang, C. Y. Liu, S. B. Wu, N. W. Liu, C. Y. Peng, T. H. Chan, C. F. Hsu, J. K. Wang, and Y. L. Wang, "Highly Raman-enhancing substrates based on silver nanoparticle arrays with tunable sub-10 nm gaps," Adv. Mater. **18**, 491-+ (2006).

75. K. Kneipp, G. R. Harrison, S. R. Emory, and S. M. Nie, "Single-molecule Raman spectroscopy - Fact or fiction?," Chimia **53**, 35-37 (1999).

76. K. Kneipp, H. Kneipp, I. Itzkan, R. R. Dasari, and M. S. Feld, "Ultrasensitive chemical analysis by Raman spectroscopy," Chem. Rev. **99**, 2957-+ (1999).

77. J. J. Baumberg, T. A. Kelf, Y. Sugawara, S. Cintra, M. E. Abdelsalam, P. N. Bartlett, and A. E. Russell, "Angle-resolved surface-enhanced Raman scattering on metallic nanostructured plasmonic crystals," Nano Lett. **5**, 2262-2267 (2005).

78. N. M. B. Perney, J. J. Baumberg, M. E. Zoorob, M. D. B. Charlton, S. Mahnkopf, and C. M. Netti, "Tuning localized plasmons in nanostructured substrates for surface- enhanced Raman scattering," Opt. Express **14**, 847-857 (2006).

79. N. M. B. Perney, F. J. G. de Abajo, J. J. Baumberg, A. Tang, M. C. Netti, M. D. B. Charlton, and M. E. Zoorob, "Tuning localized plasmon cavities for optimized surface-enhanced Raman scattering," Phys. Rev. B **76**, - (2007).

80. I. Baltog, N. Primeau, R. Reinisch, and J. L. Coutaz, "Surface-Enhanced Raman-Scattering on Silver Grating - Optimized Antennalike Gain of the Stokes Signal of 10(4)," Appl. Phys. Lett. **66**, 1187-1189 (1995).

81. M. Kahl, and E. Voges, "Analysis of plasmon resonance and surface-enhanced Raman scattering on periodic silver structures," Phys. Rev. B **61**, 14078-14088 (2000).

82. W. Knoll, M. R. Philpott, J. D. Swalen, and A. Girlando, "Surface-Plasmon Enhanced Raman-Spectra of Monolayer Assemblies," J. Chem. Phys. **77**, 2254-2259 (1982).

BIBLIOGRAPHY

83.   A. Nemetz, U. Fernandez, and W. Knoll, "Surface-Plasmon Field-Enhanced Raman-Spectroscopy with Double Gratings," J. Appl. Phys. **75**, 1582-1585 (1994).

84.   A. Kocabas, S. S. Senlik, and A. Aydinli, "Plasmonic band gap cavities on biharmonic Gratings," Phys Rev B (to be published).

85.   P. Hildebrandt, and M. Stockburger, "Surface-Enhanced resonance Raman-Spectroscopy of Rhodamine-6G adsorbed on colloidal silver," J. Phys. Chem. **88**, 5935-5944 (1984).

86.   Y. Chen, K. Munechika, and D. S. Ginger, "Dependence of fluorescence intensity on the spectral overlap between fluorophores and plasmon resonant single silver nanoparticles," Nano Lett. **7**, 690-696 (2007).

87.   N. F. Chiu, C. Yu, S. Y. Nien, J. H. Lee, C. H. Kuan, K. C. Wu, C. K. Lee, and C. W. Lin, "Enhancement and tunability of active plasmonic by multilayer grating coupled emission," Opt. Express **15**, 11608-11615 (2007).

88.   E. Takeda, M. Fujii, T. Nakamura, Y. Mochizuki, and S. Hayashi, "Enhancement of photoluminescence from excitons in silicon nanocrystals via coupling to surface plasmon polaritons," J. Appl. Phys. **102**, 023506 (2007).

89.   J. Y. Wang, Y. W. Kiang, and C. C. Yang, "Emission enhancement behaviors in the coupling between surface plasmon polariton on a one-dimensional metallic grating and a light emitter," Appl. Phys. Lett. **91**, 233104 (2007).

90.   Y. Wang, and Z. P. Zhou, "Strong enhancement of erbium ion emission by a metallic double grating," Appl. Phys. Lett. **89**, 253122 (2006).

91.   A. Yariv, Y. Xu, R. K. Lee, and A. Scherer, "Coupled-resonator optical waveguide: a proposal and analysis," Opt. Lett. **24**, 711-713 (1999).

92.   M. Soljacic, and J. D. Joannopoulos, "Enhancement of nonlinear effects using photonic crystals," Nat. Mater. **3**, 211-219 (2004).

BIBLIOGRAPHY

93. M. Soljacic, S. G. Johnson, S. H. Fan, M. Ibanescu, E. Ippen, and J. D. Joannopoulos, "Photonic-crystal slow-light enhancement of nonlinear phase sensitivity," J. Opt. Soc. Am. B **19**, 2052-2059 (2002).

94. R. S. Jacobsen, K. N. Andersen, P. I. Borel, J. Fage-Pedersen, L. H. Frandsen, O. Hansen, M. Kristensen, A. V. Lavrinenko, G. Moulin, H. Ou, C. Peucheret, B. Zsigri, and A. Bjarklev, "Strained silicon as a new electro-optic material," Nature **441**, 199-202 (2006).

95. M. Roussey, M. P. Bernal, N. Courjal, D. Van Labeke, F. I. Baida, and R. Salut, "Electro-optic effect exaltation on lithium niobate photonic crystals due to slow photons," Appl. Phys. Lett. **89**, 241110 (2006).

96. Y. A. Vlasov, M. O'Boyle, H. F. Hamann, and S. J. McNab, "Active control of slow light on a chip with photonic crystal waveguides," Nature **438**, 65-69 (2005).

97. H. Gersen, T. J. Karle, R. J. P. Engelen, W. Bogaerts, J. P. Korterik, N. F. van Hulst, T. F. Krauss, and L. Kuipers, "Real-space observation of ultraslow light in photonic crystal waveguides," Phys. Rev. Lett. **94**, 073903 (2005).

98. T. Kawasaki, D. Mori, and T. Baba, "Experimental observation of slow light in photonic crystal coupled waveguides," Opt. Express **15**, 10274-10281 (2007).

99. S. Mookherjea, and A. Yariv, "Second-harmonic generation with pulses in a coupled-resonator optical waveguide," Phys. Rev. E **65**, 026607 (2002).

100. M. Notomi, K. Yamada, A. Shinya, J. Takahashi, C. Takahashi, and I. Yokohama, "Extremely large group-velocity dispersion of line-defect waveguides in photonic crystal slabs," Phys. Rev. Lett. **87**, 253902 (2001).

101. T. Tanabe, M. Notomi, E. Kuramochi, A. Shinya, and H. Taniyama, "Trapping and delaying photons for one nanosecond in an ultrasmall high-Q photonic-crystal nanocavity," Nat. Photon. **1**, 49-52 (2007).

BIBLIOGRAPHY

102.   T. Tanabe, M. Notomi, E. Kuramochi, and H. Taniyama, "Large pulse delay and small group velocity achieved using ultrahigh-Q photonic crystal nanocavities," Opt. Express **15**, 7826-7839 (2007).   94

103.   J. K. S. Poon, J. Scheuer, Y. Xu, and A. Yariv, "Designing coupled-resonator optical waveguide delay lines," J. Opt. Soc. Am. B **21**, 1665-1673 (2004).

104.   H. Altug, and J. Vuckovic, "Experimental demonstration of the slow group velocity of light in two-dimensional coupled photonic crystal microcavity arrays," Appl. Phys. Lett. **86**, 111102 (2005).

105.   M. Bayindir, B. Temelkuran, and E. Ozbay, "Tight-binding description of the coupled defect modes in three-dimensional photonic crystals," Phys. Rev. Lett. **84**, 2140-2143 (2000).

106.   N. Stefanou, and A. Modinos, "Impurity bands in photonic insulators," Phys. Rev. B **57**, 12127-12133 (1998).

107.   A. Kocabas, S. S. Senlik, and A. Aydinli, "Plasmonic Band Gap Cavities on Biharmonic Gratings," Phys. Rev. B **2008**, 195130.

108.   J. C. Weeber, A. Bouhelier, G. C. des Francs, S. Massenot, J. Grandidier, L. Markey, and A. Dereux, "Surface-plasmon hopping along coupled coplanar cavities," Phys. Rev. B **76**, 113405 (2007).

109.   J. G. Rivas, M. Kuttge, P. H. Bolivar, H. Kurz, and J. A. Sanchez-Gil, "Propagation of surface plasmon polaritons on semiconductor gratings," Phys. Rev. Lett. **93**, 256804 (2004).

110.   M. Sandtke, and L. Kuipers, "Slow guided surface plasmons at telecom frequencies," Nat. Photon. **1**, 573-576 (2007).

111.   J. B. Khurgin, "Light slowing down in Moire fiber gratings and its implications for nonlinear optics," Phys. Rev. A **62**, 013821 (2000).

112.   O. I. Baum, and V. I. Sokolov, "Desigh of Bragg grating filters with improved spectral characteristics," in *Proc. SPIE*, S. Golubev, V., ed. (SPIE, Seventh

BIBLIOGRAPHY

International Conference on Laser and Laser-Information Technologies, 2002), pp. 511-519.

113. V. I. Sokolov, "Transmission of ultrashort light pulses through phase-shifted Bragg gratings " in *Proc. SPIE*, S. Golubev, V., ed. (SPIE, Seventh International Conference on Laser and Laser-Information Technologies, 2001), pp. 380-389.